Sideband Separating SIS receiver for 650 GHz developed by NOVA

A. Khudchenko[1,2], R. Hesper[1], A.M. Baryshev[1,3], J. Barkhof[1], J. Adema[1], M.E. Bekema[1],
L.H.R. de Haan-Stijkel[1], W.H.W.M. Boland[4]

[1]Kapteyn Astronomical Institute/NOVA, University of Groningen, Groningen, Netherlands, a.khudchenko@sron.nl
[2]Kotel'nikov Institute of Radio Engineering and Electronics RAS, Moscow, Russia
[3]Astro Space Center, Lebedev Physical Institute of Russian Academy of Science, Moscow, Russia
[4]University of Leiden/NOVA, Leiden, Netherlands

Astronomical observations for high frequencies like the Atacama Large Millimeter Array (ALMA) Band 9 (602-720 GHz) are restricted by atmospheric conditions. Because of that, for spectral line sources, the sideband separating (2SB) receiver can provide a better sensitivity than the double-sideband (DSB) one by reducing the atmospheric noise contribution. For 650 GHz window it was concluded in [1_Modular] that, in the ideal case, the 2SB/DSB sensitivity ratio can be up to 1.4 on average for spectral line sources, giving an observation time reduction factor of about 2.

In the current configuration, ALMA has 2SB receivers for frequency bands 3 through 8, i.e., for frequencies below 500 GHz. Above this range only DSB receivers were ever installed on telescopes, because of technical difficulties in the fabrication of waveguide structures. From that point of view, the instrument we present here is a pioneering development.

The design of our receiver is described in details in the papers [1,2,3,4]. The exploded view in Fig. 1 shows detains of modular approach.
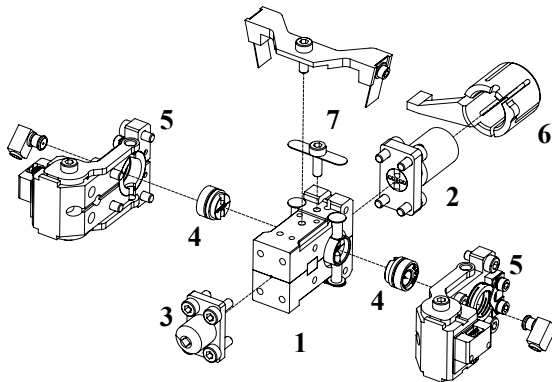
The RF part is following the classical quadrature hybrid architecture, micromachined together with local oscillator (LO) couplers and an in-phase LO splitter into a modular waveguide split block [2] shown in Fig. 2. The RF feedhorn and mixer back pieces are separate components and easily exchanged, which makes for very convenient DSB characterization of the individual mixer devices for matching purposes. The mixer devices are the same superconductor–insulator–superconductor (SIS) devices used in the current ALMA Band 9 receivers [5].

The emphasis of the RF waveguide design was placed not on ultimate phase and amplitude balance in the hybrid, but on the reduction and active suppression of reflections and standing waves. It turns out that, once the phase and the amplitude are sufficiently balanced, the image rejection ratio (IRR) starts being dominated by unbalanced parasitic reflections in the signal path, and further perfection of the hybrid's balance is not the way toward higher IRR. The description of these reflections is done in [2,3,4] and the design minimizing their effect on the receiver performance [2,4] is shown on Fig. 2.
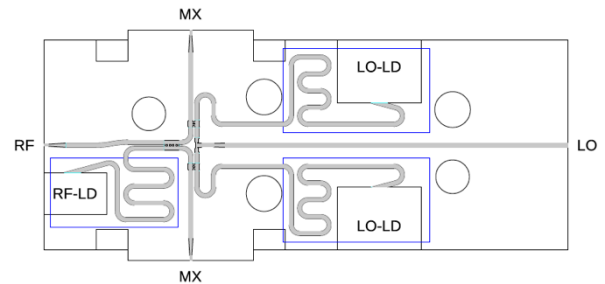

Fig. 1. Exploded view of the modular 2SB mixer block. The major parts are: "1" - a central split block (hybrid block) containing the RF waveguide structure including the loads; "2" - a corrugated RF input horn; "3" - a diagonal LO horn; "4" - two backpieces, holding one SIS device each; "5" -two side-pieces, each containing a magnet coil, most of the magnetic field conductors, heater contact, thermometer, a small PCB with a Nano-D connector to export all signals and spring-loaded retainer caps to clamp the backpieces in place; "6" - a "collet" to clamp the mixer by its horn in the optics assembly; "7" - brackets to secure connectors magnet pins and GPO connectors. Two right angle GPO connectors in right-bottom and left-top corners, show the way the IF cables are connected to the mixer block.

Fig. 2. View on the split plane of the mixer block. RF: interface to RF feedhorn, LO: LO input, MX: interface to mixer back pieces, RF-LD: cavity for RF load material, LO-LD: cavities for LO load material. The blue rectangles indicate the areas to be coated with resistive layer.

Four high-quality operational blocks were produced by GARD (Group for Advanced Receiver Development, Chalmers University of Technology, Gothenburg, Sweden). The mixers were tested in a modified copy of a standard ALMA Band 9 receiver cartridge. The noise temperature was determined with a 300/77-K hot–cold Y-factor measurement, the IRR according to the method described in [6].

The measured single-sideband (SSB) noise temperature is shown in Fig. 3. To give an idea of the noise penalty incurred by the waveguide structures, the sum of the DSB noise temperatures of the individual mixer devices is plotted as well. If all other com-

ponents were lossless, the SSB noise temperatures should correspond to this sum. In the plot, an excess noise temperature of about 20 K is observable, corresponding to about 0.5-dB loss in the waveguide structure. Overall, we roughly estimate the uncertainty of the excess noise temperature to be ±10 K. Despite this, it is clear that ALMA class specifications is met with margin.
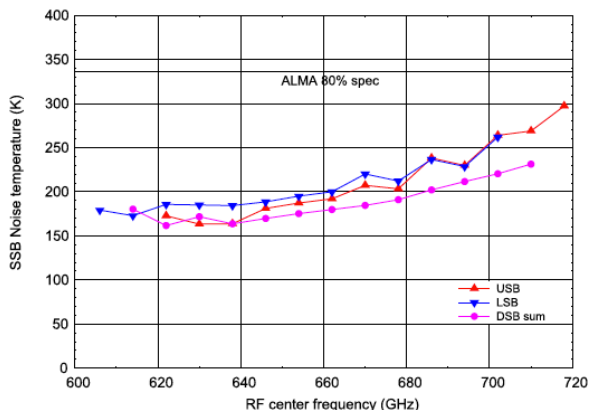

Fig. 3. SSB noise temperature of both upper and lower sidebands as a function of the RF frequency corresponding to the center of the IF band (LO + 8 GHz, LO − 8 GHz for upper sideband (USB) and lower sideband (LSB), respectively). For reference, the sum of the DSB noise temperatures of the two individual SIS mixer devices is plotted as well (average of two measurements). According to the ALMA Band 9 specifications, the SSB noise temperature should be below 336 K (horizontal line) for at least 80% of the band, and below 500 K for the entire band.

Fig. 4 shows the IRR obtained with the first production block. The IRR is above 15 dB in almost all points, with an ample margin within the typical specification (≥ 10 dB) of current receivers.

When measured image rejection traces such as in Fig. 4 are studied in detail, it is clear that apart from the obvious large-scale (order of 10 GHz) patterns resulting from residual imbalances in the RF circuit, there are persistent small-scale (subgigahertz) ripples. Because of their length scale, and their behavior when components are replaced, we attribute these to the IF system. To get an idea of the possible obtainable IRR with the current waveguide structure, provided that the IF system is improved significantly, solid curves in Fig. 4 show the IRR filtered with a 2-GHz-wide sliding window, removing most of the fast (IF-related) ripples. In this particular case, the 18-dB IRR should be obtainable over the entire band.

In conclusion, We designed, built, and tested a new 2SB mixer assembly for the 600–720-GHz band (ALMA Band 9). By concentrating on the input matching and isolation of the quadrature hybrid and associated waveguide components, rather than on the phase and amplitude balance, we minimized standing waves and especially asymmetric reflection paths, which are highly detrimental to the IRR. IRRs in excess of 15 dB are obtained repeatedly with different blocks and mixer pairs. At the same time, the SSB noise temperature is increased by not more than 20–30 K with respect to the bare mixer devices, corresponding to a loss of about 0.5 dB in the waveguide structure.
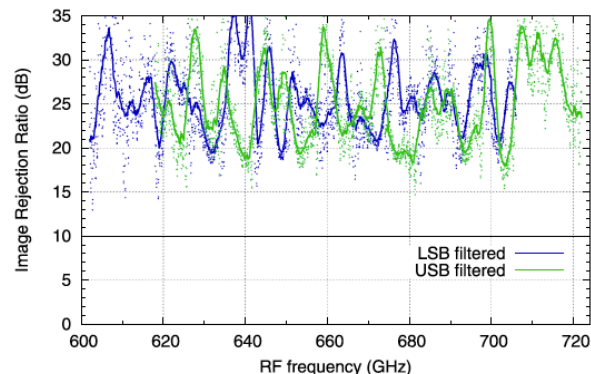

Fig. 4. IRR of the first production hybrid block as a function of RF observation frequency (i.e., the frequency of the test tone used to determine the IRR). The typical specification for 2SB ALMA bands (10-dB minimum) is indicated with a horizontal line. The dots represent the measured data. Solid curves show the filtered with a 2-GHz-wide sliding window, in order to separate the RF-induced effects from the IF-induced ones. Note, the filter is simply applied in the dB domain, not on the linear ratios.

References

1. *R. Hesper, G. Gerlofsma, F. P. Mena, M. Spaans and A. M. Baryshev, Construction of a Side Band Separating Heterodyne Mixer for Band 9 of ALMA //* Proc. 18th. ISSTT, 2007, P. 39-43.

2. *R. Hesper, A. Khudchenko, A. M. Baryshev, J. Barkhof, P. Mena, A new high-performance sideband-separating mixer for 650GHz //* Proc. SPIE, 2016, V. 9914, id. 99140G.

3. *A. Khudchenko, R. Hesper, A.M. Baryshev, J. Barkhof and F.P. Mena, Modular 2SB SIS Receiver for 600-720 GHz: Performance and Characterization Methods //* IEEE Tr. on TST, 2017, V. 7, No. 1, P. 2-9.

4. *R. Hesper , A. Khudchenko, A.M. Baryshev, J. Barkhof, and F.P. Mena, A High-Performance 650-GHz Sideband-Separating Mixer. Design and Results //* IEEE Tr. on TST. 2017, V. 7, No. 6, P. 686-693.

5. *A. M. Baryshev, et. al, The ALMA Band 9 receiver. Design, construction, characterization, and first light //* A&A, 2015, 577, A129.

6. *A. R. Kerr, S. K. Pan and J. E. Effland, Sideband Calibration of Millimeter-Wave Receivers //* ALMA memo 357, 2001.

Low-noise THz-range SIS Receivers
for Ground-based and Space Radio Astronomy

Kirill Rudakov[1,2,3], Pavel Dmitriev[1], Andrey Baryshev[2], Andrey Khudchenko[1,2],
Ronald Hesper[2], and Valery Koshelets[1].

[1]Kotel'nikov Institute of Radio Engineering and Electronics RAS, Moscow, Russia, valery@hitech.cplire.ru
[2]Kapteyn Astronomical Institute, University of Groningen, Groningen, the Netherlands
[3]Moscow Institute of Physics and Technology, Dolgoprudny, Russia

Nb-based tunnel junctions are basic elements of most low-T_c superconducting electronic devices and circuits. In particular, the superconductor-insulator-superconductor (SIS) mixers that employ high quality Nb-based tunnel junctions have the noise temperature limited only by the fundamental quantum value. That is why the SIS receivers based on high quality Nb-based tunnel junctions are currently used in both ground-based and space terahertz radio telescopes. To realize a quantum-limited performance, the SIS tunnel junctions with a high current density and extremely small leakage currents are required; this forces one to decrease junction dimensions to sub-micron level to achieve matching between such high current density junctions and antenna. Implementation of the sub-micron Nb/AlN/NbN junctions that combine high gap voltage with low leakage current at extremely high tunnel current density allows us to realize a quantum-limited performance for frequencies up to 950 GHz.

The technology for fabrication superconducting tunnel junctions Nb-AlOx-Nb and Nb-AlN-NbN with record parameters (current densities up to 100 kA/cm^2) [1-2] as well as electron-beam lithography techniques for reproducible fabrication of tunnel junctions of submicron sizes (area down to 0.1 µm^2) have been developed at Kotel'nikov Institute of Radio Engineering and Electronics. This allows to increase the operating frequency of the SIS mixers, expand their bandwidth, and create a number of ultra-sensitive receivers in the 200 -1000 GHz range [3-4], as well as develop a number of superconducting quantum interference devices for various applications. Implementation of the sub-micron Nb/AlN/NbN junctions that combine high gap voltage with low leakage current at extremely high tunnel current density allows us to realize a quantum-limited performance for frequencies up to 950 GHz.

To realize low-noise operation of the receiver at frequencies up to 1 THz the high critical current density Nb/AlN/NbN tunnel junctions were incorporated in a microstrip line consisting of a 300 nm thick bottom electrode (ground plane) made of NbTiN and a 450 nm thick top electrode made of Al [4, 5]. A cross-section of the integral receiving structure in the vicinity of a tunnel junction is shown in Fig. 1. The detailed procedure for the circuit fabrication is described in [2, 4, 5]. The NbTiN film was deposited on a fused quartz substrate at room temperature by DC sputtering with NbTi target in nitrogen atmosphere. Critical temperature T_c for the NbTiN film was measured to

be 15.1 K, and room temperature resistivity was estimated to be 85 µΩ·cm.

The twin mixing element is made by planar technology on a quartz substrate with a width of 75 µm, and consists of a triangular antenna matching the microstrip structure, a system of IF filters in the 4 ... 12 GHz band, and two SIS junctions of 0.5 µm^2 [4, 5]; a photo of the mixing element is presented in Fig. 2.

The tunnel junctions were fabricated from Nb/AlN/NbN tri-layer [2, 4] with normal state resistance-area product $R_nA = 7$ Ω·µm^2, which corresponds to current density $J_c = 30$ kA/cm^2; the Nb and NbN layers have thicknesses of 100 nm. An AlN tunnel barrier was grown immediately after deposition of a 7 nm Al layer using RF magnetron discharge. Afterwards, the NbN was deposited by DC reactive magnetron sputtering at ambient temperature. Circular-shape junctions with an area of about 0.5 µm^2 were defined by deep ultraviolet photolithography.
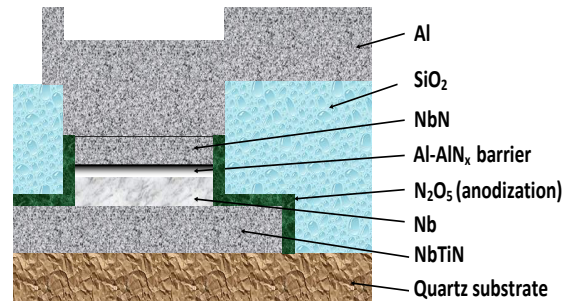

Fig. 1. Cross-section of the integrated receiving structure in the vicinity of the tunnel junction; the twin Nb/AlN/NbN junctions is inserted in the microstrip (the lower electrode is made of NbTiN with a thickness of about 300 nm, the upper electrode is made of Al with a thickness of 500 nm)

Fig. 2. Photo of the integrated mixing structure after installation in the mixer block

Optimization of technological processes made it possible to fabricate SIS transitions of submicron area ($0.5~\mu m^2$ each) and a energy gap value as high as 3.2 mV. The current-voltage characteristic of the Nb/AlN/NbN tunnel junction inserted in the integrated mixer circuit fabricated on a quartz substrate (junction area of $0.64~\mu m^2$) is shown in Fig. 3.
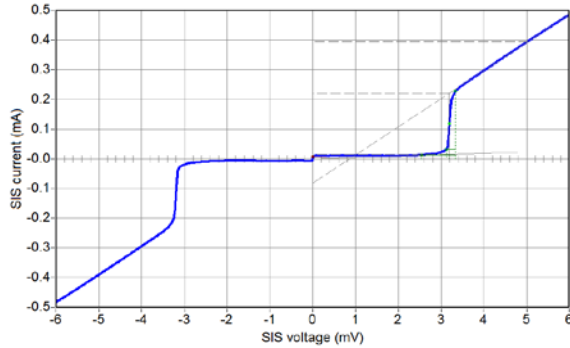

Fig. 3. IVC of the Nb/AlN/NbN SIS tunnel junction (area of $0.64~\mu m^2$) inserted in the integrated mixer circuit, which is fabricated on a quartz substrate; the critical current is suppressed by the magnetic field; Jc = 34 kA/ cm^2; Vg = 3.2 mV; Rn = 10.6 Ohm; Rj/Rn = 21.

Such parameters of the tunnel structures ensured the operation of the receiving element in a wide frequency range of 700-950 GHz, which was confirmed by studies of the Fourier transform spectrometer response of the receiving element and by measurements of its noise temperature.
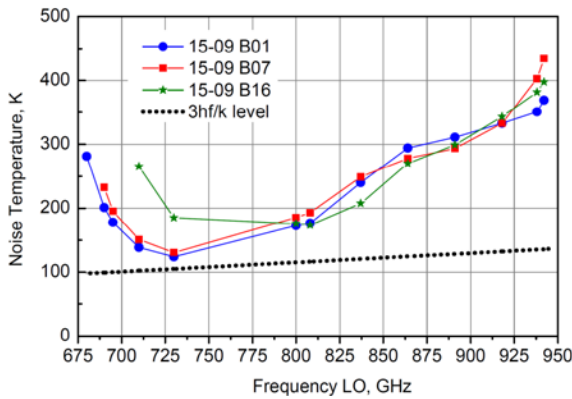

Fig. 4. Frequency dependence of the receiver noise temperature for three different tested structures. The corrected noise temperature of the receiver at a frequency of 725 GHz was 120 K, which is only 3 times the quantum limit.

The corrected noise temperature of the receiver at a frequency of 725 GHz was 120 K, which is only 3 times higher than the quantum limit hf / k$_B$; the noise temperature increases to 390 K at the top of the fre-

quency range. Dependence of the receiver noise temperature on frequency for three different structures, corrected for beam-splitter losses, is shown in Fig. 4 [4, 5]. Seven of such mixers were used for upgrade of CHAMP+ 7-pixel array and successfully installed in Chile on APEX telescope [6].

The details of the junction fabrication, as well as results of their characterization will be presented (including comparison of the tunnel barrier parameters for different fabrication procedure). Recent results of implementation of the developed sub-micron Nb-based tunnel junctions fabricated by electron-beam lithography will be presented as well. The first results on development, fabrication and testing of the Nb/AlN/NbN mixers circuits for 211- 275 GHz frequency range intended for ground-base and space telescopes will be discussed.

References

1. *P.N. Dmitriev, I.L. Lapitskaya, L.V. Filippenko, A.B. Ermakov, S.V. Shitov, G.V. Prokopenko, S.A. Kovtonyuk, and V.P. Koshelets*. High Quality Nb-based Integrated Circuits for High Frequency and Digital Applications // IEEE Trans. on Appl. Supercond.", vol. 13, No 2, pp. 107-110, 2003.

2. *M.Yu. Torgashin, V.P. Koshelets, P.N. Dmitriev, A.B. Ermakov, L.V.Filippenko, and P.A. Yagoubov,* Superconducting Integrated Receivers based on Nb-AlN-NbN circuits // IEEE Trans. on Appl. Supercond.", vol. 17, pp.379- 382, 2007.

3. *V.P. Koshelets, P.N. Dmitriev, M.I. Faley, L.V. Filippenko, K.V. Kalashnikov, N.V. Kinev, O.S. Kiselev, A.A. Artanov, K.I. Rudakov, A. de Lange, G. de Lange, V.L. Vaks, M.Y. Li, H.B. Wang,* Superconducting Integrated Terahertz Spectrometers // IEEE Transactions on Terahertz Science and Technology, vol. 5, pp 687- 694, 2015.

4. *A.V. Khudchenko, A.M. Baryshev, K.I. Rudakov, V.P. Koshelets, P.N. Dmitriev, R. Hesper, L. de Jong,* High Gap Nb-AlN-NbN SIS Junctions for Frequency Band 790-950 GHz // IEEE Transactions on Terahertz Science and Technology, vol. 6, No 1, pp. 127-132, 2016.

5. *Rudakov K. I., Paramonov M. E., Dmitriev P. N., Baryshev A. M., Khudchenko A. V., Koshelets V. P.* Analysis of high-frequency parameters of superconducting planar structures // Journal of Communications Technology and Electronics, 12(61), 1395-1399, 2016.

6. A. Khudchenko, A.M. Baryshev, R. Hesper, M.E. Bekema, R. de Haan Stijkel, J. Barkhof, D. van Nguyen, V.P. Koshelets, P. Dmitriev, M. Fominsky, K. Rudakov, S. Heyminck and R. Güsten, "Performance of SIS mixers for upgrade of CHAMP+ 7-pixel arrays", *conf. proc. 28th IS-STT*, March 2017.

Terahertz pulse detection by direct intensity modulation of the probe laser beam in GaAs

A.I. Shugurov, M. I. Bakunov

University of Nizhny Novgorod, Nizhny Novgorod, Russia, bakunov@rf.unn.ru

Introduction

Electro-optic (EO) sampling of terahertz waves by ultrashort laser pulses is a technique that is commonly used in terahertz time-domain spectroscopy. In the standard scheme of EO sampling, the probe optical pulse propagates collinearly with the terahertz pulse in an EO crystal and varies its polarization due to the Pockels effect. By measuring the polarization change as a function of the delay between the pulses, the terahertz waveform is mapped. For a given wavelength λ of the probe optical beam, an efficient EO sampling can be achieved only with a specific EO crystal that provides optical-terahertz velocity matching. For example, ZnTe is routinely used to perform EO sampling by a Ti:sapphire laser ($\lambda \approx 0.8\ \mu$m).

Unfortunately, there is no crystal, which could provide velocity matching at the wavelength ($\lambda \approx 1.55\ \mu$m) of femtosecond fiber lasers. Meanwhile, such lasers are a promising light source for low-cost compact terahertz spectrometers. To circumvent velocity mismatch, non-collinear propagation of the optical and terahertz pulses in an EO crystal can be used. In particular, the probe optical beam should propagate at the Cherenkov angle to the terahertz beam. Non-collinear extensions of the standard ellipsometric EO sampling were demonstrated with fiber lasers in LiNbO$_3$ [1] and GaAs [2] crystals.

Recently, a non-collinear non-ellipsometric method of EO sampling has been proposed [3]. In this method, terahertz field is detected by measuring the intensity modulation of the probe optical beam without any polarization optics. The modulation appears as a result of non-collinear propagation of the probe beam parts, which are oppositely modulated via the sum- and difference-frequency-generation processes [4]. The method was experimentally demonstrated by using a Si-prism-coupled LiNbO$_3$ crystal [3].

Here, we implement non-collinear non-ellipsometric EO sampling in a GaAs crystal. Due to a smaller, than in LiNbO$_3$, velocities mismatch between optical and terahertz waves in GaAs, we avoid using any coupling optics, unlike Ref. [3].

Experimental

The experimental setup is shown in Fig. 1. A femtosecond fiber laser ($\lambda = 1.55\ \mu$m, 70 fs pulse duration, and 100 MHz repetition rate) was used as an optical source. The laser beam was split into the pump beam (35 mW power), which triggered a photoconductive antenna (PCA), and probe beam (30 mW) whose power was adjusted by using a half-wave plate ($\lambda/2$) and Glan prism (GP). By means of a TPX lens

and a parabolic mirror, the terahertz beam was collimated and focused to a spot of a 1.2 mm width on the entrance surface of an 1-cm thick <110>-cut GaAs crystal. The probe optical beam was collimated by lens f_1 with a 25.4 mm focal length and focused onto the GaAs crystal by lens f_2, whose focal length was varied to provide different beam widths in the crystal. The setup could be switched from the non-ellipsometric operation mode to the ellipsometric one [2] by using a flipped mirror (it required also rotating the GaAs crystal by 90°). In the ellipsometric operation mode, a standard combination of a quarter-wave plate ($\lambda/4$) and a Wollaston prism (WP) was used to measure the polarization variation of the probe beam. In the non-ellipsometric scheme, a D-shape mirror was used to divide the beam into two halves and direct them to a balanced photodetector. To minimize water vapor absorption, the measurements were made in dry air conditions.
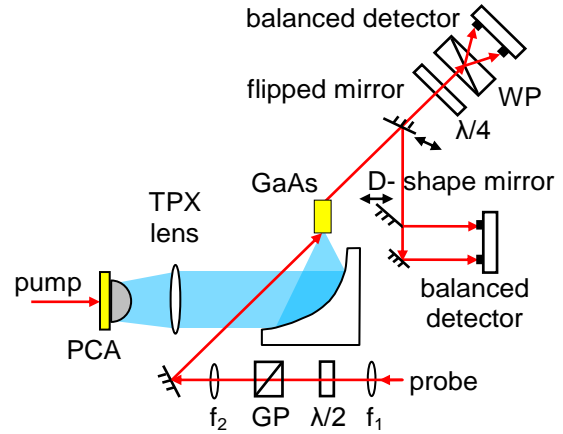

Fig. 1. Schematic of the experimental setup.

Results and discussion

Figure 2 shows the EO signals [Fig. 2(a)] and corresponding spectra [Fig. 2(b)], which were obtained by using the non-ellipsometric method for different widths (80, 120, 180, and 500 μm) of the probe beam. The curves obtained with the standard ellipsometric method (with an 80-µm wide probe beam) are shown for reference. According to Fig. 2, the detection efficiencies of the ellipsometric and non-ellipsometric methods are comparable, although the signal shapes are different. For the 80-μm wide beam, the shape of the non-ellipsometric signal is close to the time derivative of the ellipsometric signal [inset in Fig. 2(a)]. For wider beams, the non-ellipsometric signal becomes smoother.
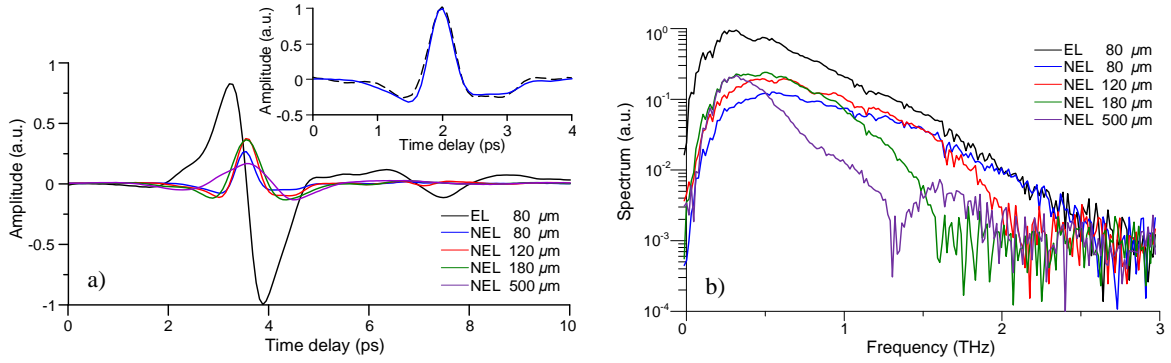
Fig. 2. (a) EO signals and (b) corresponding terahertz spectra obtained by the non-ellipsometric (NEL) method with different widths of the probe beam. The signal and spectrum obtained by the ellipsometric (EL) method are shown for reference. Inset: normalized NEL 80 μm signal (solid) in comparison with the time derivative of the EL signal (dashed).

The spectra in Fig. 2(b) confirm the theoretical prediction [4] that the non-collinear non-ellipsometric scheme operates as a bandpass filter, whose transmission band depends on the probe beam width. In particular, for the 500-μm wide beam, the scheme operates as a low-pass filter, which attenuates high frequencies. Physically, it can be explained by the fact that in non-collinear configuration different parts of the pancake-shaped probe pulse interact with different phases of the terahertz field, thus reducing the EO response [2]. The effect is more pronounced for a wider probe beam and smaller terahertz wavelengths. For the 80-μm wide beam, on the contrary, low frequencies are filtered out whereas high frequencies are boosted [Fig. 2(b)]. The optimal width of the probe beam, which allows one to measure correctly the spectrum of the used terahertz source is ~120 μm [Fig. 2].
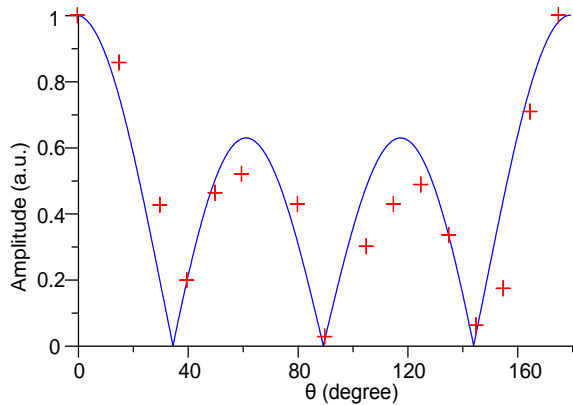

Fig. 3. The output non-ellipsometric signal as a function of θ: experiment (crosses) and theory (solid line).

To maximize the efficiency of the non-ellipsometric scheme, the polarizations of the terahertz and optical beams should be different from those in the ellipsometric scheme. In particular, the maximal efficiency is achieved when the polarizations are parallel each other and directed at ≈55° to the [001] axis [5]. This configuration is not, however, convenient for practical use. Instead, we propose to use the configuration with the [001] axis aligned along the terahertz beam polarization and orthogonal to the optical beam polarization. To corroborate this prediction, we derived the dependence of the output non-ellipsometric signal ΔI on the crystal rotation angle θ for fixed polarizations of the optical and terahertz fields. This dependence reads as

$$\Delta I \sim \cos\theta(2 - 3\cos^2\theta) \qquad (1)$$

And agree well with the experimental results [Fig. 3].

Conclusion

We have experimentally demonstrated efficient broadband EO sampling of terahertz pulses in a GaAs crystal without any polarization, contrary to Ref. [2], and coupling, contrary to Ref. [3], optics. Our results confirm the theoretical predictions of Ref. [4].

References

1. *Tani, M. et al.* Efficient electro-optic sampling detection of terahertz radiation via Cherenkov phase matching// Opt. Express. 2011. V. 19, No. 21. P. 19901–19906.

2. *Mashkovich, E. A. et al.* Noncollinear electro-optic sampling of terahertz waves in a thick GaAs crystal// IEEE Trans. THz Sci. Technol. 2015. V. 5, No. 5. P. 732–736.

3. *Tani, M. et al.* Non-ellipsometric detection of terahertz radiation using heterodyne EO sampling in the Cherenkov velocity matching scheme// Opt. Express. 2013. V. 21, No. 8. P. 9277–9288.

4. *Bakunov, M. I., Gorelov, S. D., Tani, M.,* Nonellipsometric noncollinear electrooptic sampling of terahertz waves: A comprehensive theory// IEEE Trans. THz Sci. Technol. 2016. V. 6, No. 3. P. 473–479.

5. *Kovalev, S. P., Kitaeva, G. K.,* Terahertz electrooptical detection: optical phase or energy measurements// J. Opt. Soc. Am. B. 2013. V. 30, No. 10. P. 2650–2656.

Imaging of powerful terahertz beams

I. V. Andreev, V. M. Muravev, A. R. Khisameeva, G. E. Tsydynzhapov, I. V. Kukushkin

MWAVE LLC, Moscow, Russia, ivan.andreev@terasense.com

THz frequency range is a field of constantly growing interest within modern applied physics. Non-destructive imaging, time-domain and frequency domain spectroscopy in THz range become important up-to-date techniques of material characterization [1]. Recently considerable interest was attracted by various THz personnel screening and security systems. Powerful THz sources, such as gyrotrons, could be used as a focused heating source for selective melting with controllable temperature distribution in glass and semiconductor industry [2], or for plasma heating into ITER tokamak. Lots of existing applications require quasi-optical setup, which demands proper beam alignment and focusing. Sometimes it becomes a complicated task since sub-THz radiation is invisible to the eye. We developed THz square cameras, which allows for real-time beam profiling of various vacuum-tube and semiconductor-based THz sources and could greatly simplify adjustment of quasi-optical setups. Cameras are suitable for both vacuum-tube (BWO, gyrotrons) and semiconductor-based (IMPATT and Gunn diodes) THz sources operating in range of 50–700 GHz.

Our group have developed a new semiconductor-based technology for detection of THz radiation in a broad range of 50–700 GHz. Detectors are fabricated from GaAs/AlGaAs quantum well heterostructures with high two-dimensional (2D) electron conductivity. Detection principle is rest on coupling of incident sub-THz radiation to so-called relativistic plasmons in 2D electron system [3] and subsequent rectification of plasmon ac potential on nonlinear defects, which provides a dc signal at the output of the detector. Single detector itself has a noise equivalent power (NEP) of 0.5 nW/Hz$^{1/2}$ and ultrafast response time of 120 ps. GaAs detectors are fully compatible with common semiconductor processing lines, which makes them comparatively inexpensive, and allows to manufacture detectors on industrial scale and with reproducible properties.

Further to our research, we are developing a graphene-based detector in THz frequency range. Plasma oscillations in graphene have typical frequencies in THz range, which allows graphene to be used as a detector in this range of electromagnetic radiation. This material has the highest value or 2D electron mobility that provides high 2D conductivity and allows to observe weakly damped relativistic plasma oscillations. In contrast to common two-dimensional plasmons, the damping of relativistic plasma mode [3] is not determined by the inverse time of scattering of charge carriers. Thanks to weak damping, these plasma oscillations can be excited even at room temperature when ordinary plasmons are strongly suppressed. Compared to existing analogs, the plasmon detector based on graphene should have the highest responsivity and fastest response time.

Fig. 1. Visual appearance of a Tera-4096 square imaging camera (64x64 pixels, 96x96 mm^2 active area size).

Ownership of the detector technology allowed us to develop a line of THz imaging cameras (Fig. 1). Camera consists of a focal plane array of detectors (pixels), combined with amplification and readout circuitry. Cameras have a modular design, being assembled from blocks, which provides a very good scalability in pixel number and imaging area size. Most common camera sizes are 16x16, 32x32 and 64x64 pixels. High frame rate (up to 90 fps) makes possible to perform a real-time THz imaging. Typical camera parameters are summarized in the table below.

Frequency range	50 – 700 GHz
NEP	1 nW/Hz$^{1/2}$
Frame rate	0.2 – 90 fps
Typical pixel number	16x16, 32x32, 64x64
Pixel size	1.5x1.5 or 3x3 mm^2
Features	Mini-USB interface, TTL sync out

As well as square cameras with frame rate not more than 100 fps, TeraSense also manufactures fast linear cameras with frame rate up to 5000 lines per second. Linear cameras are targeted at conveyor-belt based scanning applications.

TeraSense cameras proved itself as a flexible solution in a number of applications, such as non-destructive testing and quality control in industrial manufacturing lines [4], especially in area of humidity control in dry materials, mail inspection and security screening. Another promising application of THz imaging cameras is real-time beam profiling in various quasi-optical setups [5].
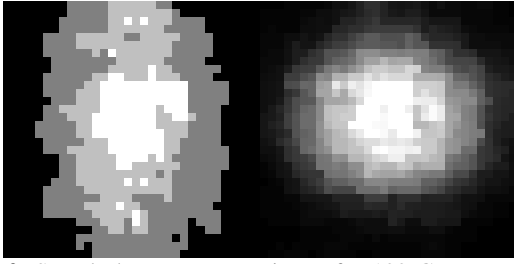
Fig. 2. Sample beam cross-sections of a 100 GHz source, taken with Tera-1024 32x32 pixel camera for two different output geometries. Left: WR8 rectangular waveguide. Right: conical horn.

Square cameras could capture a cross-section power distribution of a beam less than in one second. This simplifies beam alignment procedure, makes possible to control angular pattern of the source, and solve other tasks arising in everyday life of experimental physicists and engineers working with quasi-optical THz setups. Cameras are broadband sensitive in 50–700 GHz frequency range with several sensitivity peaks, which positions could be adjusted and optimized at the manufacturing stage. Minimal detectable power depends on the frame rate and is about $1\mu W/cm^2$ at 1 fps, which allows cameras to operate even with low-power sources. Spatial resolution (discretization) of the beam cross-section image is limited by the pixel size and could be 1.5 or 3 mm. Fig. 2 demonstrates sample beam cross-section images of the same source for various output geometries. Cameras could be used for alignment not only continuous-wave, but pulsed beams as well. Operating with the pulsed beam, camera resembles mean beam power distribution. Camera pixels are tolerant to powerful beams, allowing to work not only with semiconductor-based sources, but with high-power vacuum-tube sources as well.

References

1. *Zhang, H., Sfarra, S., Saluja, K., Peeters, J., Fleuret, J., Duan, Y., Fernandes H., Avdelidis N., Ibarra-Castanedo C., Maldague, X.* Non-destructive investigation of paintings on canvas by continuous wave terahertz imaging and flash thermography // Journal of Nondestructive Evaluation. 2017. V. 36, No. 2. P. 34.

2. *Sklyarevich V., Shevelev M.* Method for the rapid thermal treatment of glass and glass-like materials using microwave radiation. // U.S. Patent No. 6,408,649. 25 Jun. 2002.

3. *Muravev, V. M., Gusikhin, P. A., Andreev, I. V., Kukushkin, I. V.* Novel relativistic plasma excitations in a gated two-dimensional electron system // Physical review letters. 2015. V. 114. No. 10. P. 106805.

4. *Zhang, H., Sfarra, S., Sarasini, F., Santulli, C., Fernandes, H., Avdelidis, N. P., Ibarra-Castanedo C., & Maldague, X. P.* Thermographic non-destructive evaluation for natural fiber-reinforced composite laminates // Applied Sciences. 2018. V. 8. No. 2. P. 240.

5. *Yıldırım, İ. O., Özkan, V. A., İdikut, F., Takan, T., Şahin, A. B., & Altan, H.* Characterization of a terahertz wave scanned imaging system for threat detection at stand-off distances // Optical and Quantum Electronics. 2016. V. 48. No. 7. P. 367.

Optical-Mechanical Analogy Approach for the Purposes of Detection of IR-MW Radiation

A.V. Bogatskaya[1,2,3], N.V. Klenov[1,3,4,5], M.V. Tereshonok[3,5] and A.M. Popov[1,2,4]

[1]D. V. Skobeltsyn Institute of Nuclear Physics, Moscow State University, Moscow, Russia, annabogatskaya@gmail.com
[2]P. N. Lebedev Physical Institute, RAS, Moscow Russia
[3]Moscow Technical University of Communication and Informatics, 111024, Moscow, Russia
[4]Department of Physics, Moscow State University, 119991, Moscow, Russia
[5] Moscow Technological University (MIREA), 119454, Moscow, Russia

Here we propose a generalized physical approach providing possible technical realizations of a number of urgent problems related to the interaction of electromagnetic radiation with plasma and conducting media. Proposed approach is based on the use of well-known optical-mechanical analogy which exploit mathematical identity of the stationary Schroedinger equation in quantum mechanics for the particle motion in potential field and Helmholtz equation in wave theory.

Let us consider spatially inhomogeneous non-magnetic medium characterized by the susceptibility $\chi(\vec{r})$, or permittivity $\varepsilon(\vec{r}) = 1 + 4\pi\chi(\vec{r})$. In the case of monochromatic field $\vec{E} = \vec{E}_0(\vec{r})\exp(-i\omega t)$ ($\vec{H} = \vec{H}_0(\vec{r})\exp(-i\omega t)$, ω is the radiation frequency) Maxwell equations for electric and magnetic field strength can be written as:

$$rot\,\vec{E} = \frac{1}{c}i\omega\vec{H}, \quad div(\varepsilon\vec{E}) = 0,$$
$$rot\,\vec{H} = -\frac{\varepsilon}{c}i\omega\vec{E}, \quad div\,\vec{H} = 0. \tag{1}$$

From (1) one can obtain the following equation for electric field strength $\vec{E}$:

$$\Delta\vec{E} + \nabla\left(\frac{1}{\varepsilon}(\vec{E}\nabla)\varepsilon\right) + \frac{\varepsilon\omega^2}{c^2}\vec{E} = 0. \tag{2}$$

For the case when permittivity depends only on one spatial coordinate $\varepsilon = \varepsilon(z)$ and wave field propagates alone this direction the equation (2) transforms to the well-known Helmholtz equation for the spatial distribution of electric field strength E:

$$\frac{d^2E}{dz^2} + k_0^2(1 + 4\pi\chi(z))E = 0. \tag{3}$$

with $k_0^2 = \omega^2/c^2$. Here electric field propagates in the direction perpendicular to z-axis.

Equation (3) is mathematically equivalent to the stationary Schrödinger equation in quantum mechanics for the particle wave function $\psi(z)$ in the potential field $V(z)$:

$$\frac{d^2\psi}{dz^2} + \kappa_0^2\left(1 - \frac{V(z)}{\zeta}\right)\psi = 0, \tag{4}$$

where $\kappa_0^2 = 2m\zeta/\hbar^2$ is the wave vector of the particle with energy ζ. Direct comparison of eq. (3) and (4) leads to the conclusion that potential function $V(z)$ in quantum mechanics is similar to the susceptibility in electromagnetic theory $(2m/\hbar^2)V(z) \to (1-\varepsilon)\cdot(\omega/c)^2 = -4\pi\chi(z)\cdot(\omega/c)^2$. Thus the eigenvalue problem for the Hamiltonian in quantum theory turns out to be mathematically identical to the problem of calculating the stationary distribution of the electric field strength in a wave. The medium with $\varepsilon > 0$ can be associated with an attractive potential $V(z) < 0$ (potential well) while the medium with $\varepsilon < 0$ acts as potential barrier $V(z) > 0$. In particular, the transport of the electron flux in heterostructures is mathematically identical to the problem propagation of electromagnetic waves through inhomogeneous media.

If the potential curve $V(z)$ has the piecewise-continuous structure (Fig. 1), both the ψ-function and its derivative $d\psi/dx$ should be continuous functions in the potential breaking points. Similar boundary conditions appear to exist in electromagnetic theory: the tangential components of $\vec{E}, \vec{H}$ should also be continuous functions at the interface regions. Using Maxwell equations one can rewrite the boundary conditions as the continuity of tangential components of $\vec{E}$ and its derivative. For the normal incidence when only tangential components of $\vec{E}, \vec{H}$ have the non-zero values these boundary conditions are equivalent to boundary conditions for the wave function in quantum mechanics. The above conclusion known as an optical-mechanical analogy in quantum theory gives rise to a lot of practical applications and transfer the quantum theory problem solutions to optics and vice versa.

We perform an analysis of the possibility of penetration of electromagnetic waves through opaque media using the analogy of tunneling of a quantum-particle flux through a potential barrier with a height greater than its kinetic energy. As an example, we consider plasma sheath surrounding the hypersonic vehicle as a potential barrier and analyze the overcoming of radiocommunication blackout problem [1].

Really, for the collisionless plasma the permittivity reads $\varepsilon_p = 1 - \omega_p^2/\omega^2$, where $\omega_p^2 = 4\pi e^2 n_e/m$ is the plasma frequency squared and n_e is the electron density. From this point of view the plasma sheath appearing around the hypersonic vehicle during the

flight looks like a potential barrier for the target transmission frequencies less than plasma frequency.
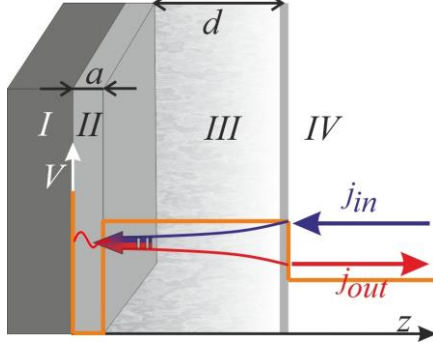

Fig. 1. The concept of overcoming of radio communication blackout: profile of the "potential barrier" $V(z) \leftrightarrow (1 - \varepsilon(z))$ containing a vehicle surface (I), dielectric layer (thickness a) with embedded antenna (II) and plasma sheath (III). (IV) corresponds to the region of infinite motion of the electromagnetic wave (atmospheric air).

The main idea is to embed a «resonator» (it can be a dielectric layer with rather large value of permittivity ε_d) between the surface on the vehicle and plasma sheath which is supposed to provide an effective tunnelling of the signal to the receiving antenna. Calculations (see Fig.2) show sharp increase of tunnelling probability of electromagnetic signal if the frequency of incident radiation coincides with the eigen-frequency of resonator (dielectric layer) which is determined by formula $\omega_n \approx \dfrac{\pi c}{a\sqrt{\varepsilon_d}} n$, $n = 1,2,3...$. Here we introduce the filling factor $F(f)$ which represents the degree of resonator filling by the incoming radiation flux:

$$F(f) = \max\left\{ |E_d|^2 / |E_{a+}|^2 \right\}, \qquad (5)$$

where $|\vec{E}_d|^2$ and $|\vec{E}_{a+}|^2$ are the squared absolute values of electric field strength in dielectric layer and air correspondingly.
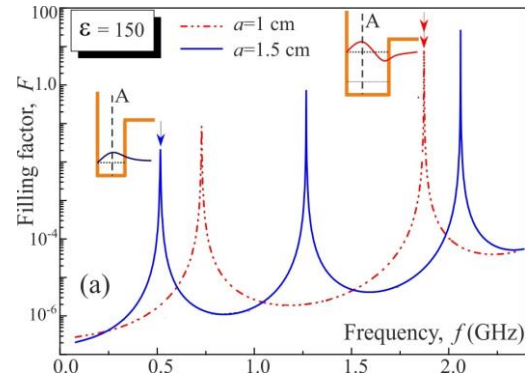

Fig. 2. The filling factor $F(f)$ in dependence on the transmitted signal frequency (normal incidence on vehicle surface). Calculations are made for $d = 10$ cm and $\varepsilon_d = 150$. The inset to figure schematically represents parts of the corresponding wave functions of stationary states within the framework of the optical-mechanical analogy.

The role of collisions in plasma as well as cases of normal and oblique incidence of radiofrequency waves on the vehicle surface are studied in [1].

One more promising application of the suggested approach implies a method for increasing the efficiency of bolometric photodetectors. The results of calculations show that by choosing thickness and dielectric constant of the substrate-resonator under a thin layer of metal (superconductor) one could bring the fraction of absorbed radiation in the detector to a value close to unity at a certain frequency of the infrared range [2].

References

1. Bogatskaya A. V., Klenov N. V., Tereshonok M. V., Adjemov S. S., Popov A. M. // J. Phys. D. 2018. V. 51, P. 185602.
2. Bogatskaya A. V., Klenov N. V., Tereshonok M. V., Popov A. M. // *Technical Physics Letters* 2018. V.44, № 8, p. 667–670

Efficient electron cooling in Cold Electron Bolometers

A.V. Gordeeva[1,2], A.L. Pankratov[1,2], V.O. Zbrozhek[1],

A.V. Blagodatkin[1,2], L.S. Revin[1,2], D.A. Pimanov[1], L.S. Kuzmin[1,3]

[1]Nizhny Novgorod State Technical University n.a. R.E. Alekseev, Nizhny Novgorod, Russia, anna.gord@list.ru
[2]Institute for Physics of Microstructures of RAS, Nizhny Novgorod, Russia
[3]Chalmers University of Technology, Gothenburg, Sweden

We have reached experimentally a theoretical minimum of electron cooling in Cold Electron Bolometer at base temperature 300 mK. The efficiency of the cooling depends on how the removal of hot quasiparticles from the vicinity of the tunnel barrier is organized. By double stock and traps for hot quasiparticles we have managed to make the removal of the hot quasiparticles as efficient as 99%. We also explain such high efficiency by the absence of Andreev reflections due to hybrid superconductor/ferromagnet structure for absorber.

The superconductor-insulator-normal metal (SIN) tunnel junctions are known for their ability to remove heat from the electron system of the normal metal electrode. Two SIN junctions, connected in SINIS structure, remove the heat twice more efficiently than a single junction [1]. This property is intensively used in Cold-Electron Bolometers [2,3], where normal metal serves as an absorber of incoming signal.

The maximum cooling by 200 mK was demonstrated in several groups, for example, from 300 mK to 100 mK in [4]. However, the theory predicts that the electron system can be cooled even lower down to 70 mK.

The efficiency of the cooling depends on how the removal of hot quasi-particles from the vicinity of the tunnel barrier is organized. In SINIS structures if hot quasi-particles stay near the barrier in S-electrodes, some power may return back to the normal metal through the phonon system or due to backtunneling.

We present three types of cold electron bolometers with different cooling efficiency. We start from the first design, when about 30% of the heat, removed through the SIN junctions, return back to the absorber. Then we describe the second and the third designs with improvements, that made the return power to decrease from 30% to 6% and finally to just 0.5%. Thus, we remove the hot quasiparticles from the vicinity of the tunnel barrier in the most effective possible way.

The tunneling current in SIN junction is given by the well known expression:

$$I = 1/(eR_T) \int \nu(\varepsilon) \left[f((\varepsilon - eV)/\tau_E) - f(\varepsilon/\tau_S) \right], \qquad (1)$$

where V - voltage drop across one SIN junction, R_T - normal state resistance of SIN junction, $\nu(\varepsilon)$ - density of states in superconductor, $f(\varepsilon)$ - Fermi-Dirac distribution, τ_E and τ_S are electron temperatures in normal metal and in superconductor, respectively. We use the expression (1) to restore electron temperature in the

normal absorber together with the heat balance equation, as described, for example, in [5]. The current I, voltage V and R_T are determined experimentally, τ_S does not influence the result and can be set to the phonon temperature. Thus, only τ_E remains unknown quantity in this expression.

The electron temperatures, found from (1), are shown in Fig. 1 and Fig. 2 on right axis. Normal resistance of the measured samples varies from 0.7 to 1.6 kΩ. The samples are made of aluminum with critical temperature 1.24 K.

In Fig.1 we compare a sample with a single connection of superconducting electrode to the thermal bath with a sample, which has two connections to thermal bath for each superconducting electrode. One can see a dramatic increase in electron cooling for the second sample. The better cooling efficiency is seen on IV-curves as increasing superconducting gap. We have measured the critical temperatures of superconducting electrodes for all our samples and found that it was 1.47 K for the first sample and 1.24 K for the second one, i.e. it would have opposite effect. Therefore, the change in IV-curves is due to different electron temperatures in the absorber.

We note that the first sample was expected to show good cooling properties as well due to implementation of normal metal traps below the superconducting electrodes. But as appears, the double stock works much more effectively than the single stock with traps.
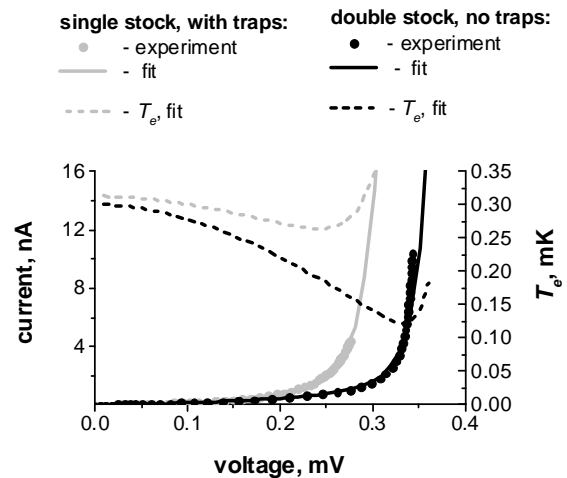

Fig. 1. Left axis: IV-curves of two bolometers with different configuration of superconducting electrodes. Right axis: electron temperatures of the absorbers. The phonon temperature is 300 mK for both bolometers.

In Fig. 2 we compare the second sample from Fig. 1 with a sample, which has both double stock and traps. Again we can see a significant improvement in cooling properties for the latter sample (black colour).

Now let us point out another possible reason of reaching the minimal electron temperatures, namely suppression of Andreev reflection. It was shown in [6] that two-particle current due to Andreev reflection generates Joule heating in normal electrode, restricting the cooling effect at low temperatures. In our samples we use sublayer of Fe in order to suppress superconductivity in aluminum, used as a normal metal absorber. We suppose that this thin layer of ferromagnet reduces the Andreev currents in our samples.

Thus, by double stock, by traps for hot quasi-particles and by suppression of Andreev current we manage to make the self cooling as efficient as possible. The suppression of Andreev current is organized using hybrid superconductor/ferromagnet structure for the absorber.
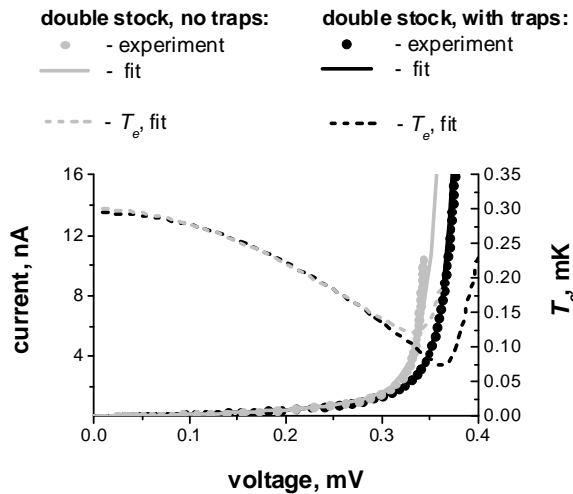
Fig. 2. Left axis: IV-curves of two bolometers without and with normal metal traps below the superconducting electrodes. Right axis: electron temperatures of the absorbers. The phonon temperature is 300 mK for both bolometers.

References

1. *Nahum M., Eiles T. M. and Martinis J. M.* Electronic micro-refrigerator based on a NIS tunnel junction // Appl. Phys. Lett. 1994. V. 65. P. 3123.

2. *Kuzmin L.* Ultimate Cold-Electron Bolometer with Strong Electrothermal Feedback // Proceedings of SPIE. 2004. V. 5498. P. 349.

3. *Kuzmin L.* An Array of Cold-Electron Bolometers with SIN Tunnel Junctions and JFET readout for Cosmology Instruments // Journal of Physics: Conference Series. 2008. V. 97, P. 012310.

4. *Leivo, M.M., Pekola, J.P. and Averin, D.V.* Microrefrigeration by NIS tunnel junctions // Czech J Phys. 1996. V. 46(Suppl 5): P. 2763.

5. *Gordeeva,A.V., et al.* Observation of photon noise by cold-electron bolometers // Appl. Phys. Lett. 2017. V. 110. P. 162603

6. *Vasenko A.S., Bezuglyi E.V., Courtois H., Hekking F.W.J.* Electron cooling by diffusive normal metal–superconductor tunnel junctions // Phys. Rev. B. 2010. V. 81. P. 094513.

Terahertz Electro-Optic Sampling in Crystals with High Natural Birefringence

I.E. Ilyakov[1,2,3], G.Kh. Kitaeva[4], B.V. Shishkin[1,2], and R.A. Akhmedzhanov[1]

[1]Institute of Applied Physics RAS, Nizhny Novgorod 603950, Russia, i.ilyakov@hzdr.de
[2]N.I. Lobachevsky State University of Nizhny Novgorod, Nizhny Novgorod 603950, Russia
[3]Helmholtz-Zentrum Dresden-Rossendorf, Bautzner Landstr. 400, 01328 Dresden, Germany
[4]M.V. Lomonosov Moscow State University, Faculty of Physics, Moscow 119991, Russia

The femtosecond lasers allows one to generate via various nonlinear processes pulsed terahertz wave radiation (0.1-10 THz) with unique characteristics: subpicosecond duration containing only one-two periods of oscillation and extremely wide spectrum. These terahertz pulses are in demand for different applications which is supported also by sensitive optical methods of coherent detection. In recent years, great progress was made in the laser-to-terahertz pulse conversion efficiency using highly nonlinear organic materials and lithium niobate (LN) crystal structures [1, 2]. In spite of high conversion efficiencies obtained during generation process there is a lack of data about efficient use of this crystals and crystal structures as detectors. The main reason is that their application in the most popular standard electro-optic (EO) detection set up based on Pockels effect [3] is hindered by decoherence of the laser polarization components because of high natural birefringence of these crystals [4]. In this work we perform the detection methods suited to be used with EO crystals with various natural birefringence and test experimentally their applicability with different EO crystals and crystal structures.

When the laser pulse interacts with THz in EO crystal not only its polarization ellipticity but also its energy could be changed [5, 6]. These changes depend on the amplitude and phase of the THz overlapped with the laser pulse and can be used for terahertz time-domain measurements [5, 6]. The method based on energy changes can separately measure the energies of the orthogonal polarization components of the laser pulse and, in contrast to techniques based on ellipticity changes, does not require maintaining coherence between the polarization components and thus, can be used with birefringent crystals.

The sensitivity of both the "energy-based" method and the standard "ellipticity-based" one can be improved if the laser pulses with the edge-cut spectrum are used. As we shown theoretically [7, 8] the relative changes of spectral energy density and ellipticity at the frequencies corresponding to the edge-cut of the laser pulse spectrum could be much higher than when a laser pulse with Gaussian spectrum is used. To realize this in experiment an edge filter can be positioned before the EO crystal to produce the high gradient of the spectral energy density of the laser pulse and the laser pulse after interaction with THz in the EO crystal can be decomposed in the frequency spectrum by a diffraction grating or can be passed through another edge filter transmitting only the optical waves with frequencies corresponding to the slope of the first filter [7, 8].

These techniques were tested in our experiments with a number of crystals [7-10]: with ZnTe and GaP - commonly used for EO sampling, and with birefringent ones – periodically-poled LN (PPLN) and DSTMS crystals. All of them demonstrated an applicability of being used with the suggested methods.
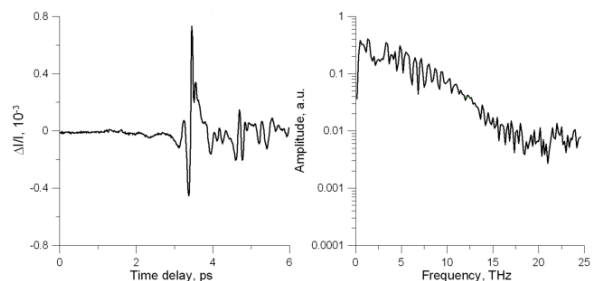

Fig.1. THz wave form and amplitude spectrum measured by DSTMS crystal.

In its easiest configuration the technique based on the total laser pulse energy changes demands even fewer optical elements than the standard one. It was tested as for narrow band detection with PPLN crystal, which allows one to achieve optical-THz synchronism at various terahertz frequencies and laser wavelengths. Application of this method with DSTMS crystal led to significant broadening of the detection bandwidth. The THz waves with frequencies up to 15 THz could be measured by the laser pulses with duration of 50 fs (Figure 1). However, for the same crystal – ZnTe or GaP this technique demonstrates the lower sensitivity than the standard one.

To improve the sensitivity of measurements the techniques with edge-pass filters were used [7, 8]. At high frequencies they demonstrated more than an order higher sensitivity comparing with the standard detection technique when the same ZnTe and GaP detection crystals were used. Further improvement of the detection sensitivity and bandwidth was achieved with the PPLN (Figure 2) and DSTMS crystals. The use of DSTMS crystal also demonstrated higher bandwidth comparing with the use of GaP crystal.

The sandwich structures with LN core demonstrated previously the high optical-terahertz conversion efficiency [11]. The use of these structures for noncollinear EO sampling was demonstrated previously basing on the spatial modulation of the laser power density [12]. However, due to the less sensitivity of this technique the signal was lower
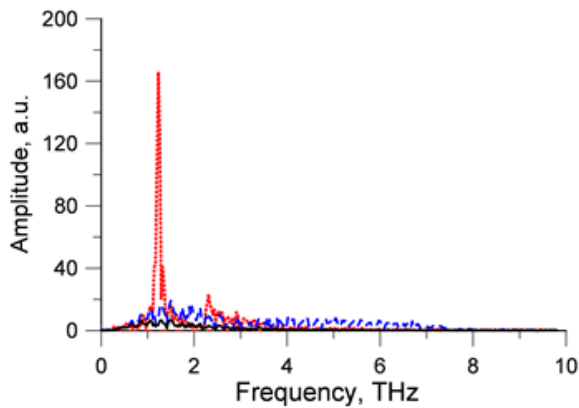
13

Fig.2. Fourier amplitude spectra of time dependences measured by the standard measurement scheme with the GaP crystal (black-solid line); by the scheme with edge filters and the GaP crystal (blue-dashed line) and with the PPLN crystal (red-dotted line, highest curve).

comparing with the standard one. Our future plan is to combine such structures with the detection methods described above. Due to the noncollinear detection scheme with a Si prism coupling it is possible to achieve a broadband optical-THz synchronism in LN and reduce the wavelength absorption. The detection sensitivity significantly depends from the probe pulse width. However, for the suggesting method with the edge filters we can take only the part of the optical beam after the crystal and reduce by this way the effective transverse area of the optical-THz interaction. As is seen from the Figure 3, the detection bandwidth and detection sensitivity could be much higher than the ones of the standard detection technique with the ZnTe crystals of various thicknesses. The calculation results of the detection sensitivity at different probe beam diameters will be also presented in the report.
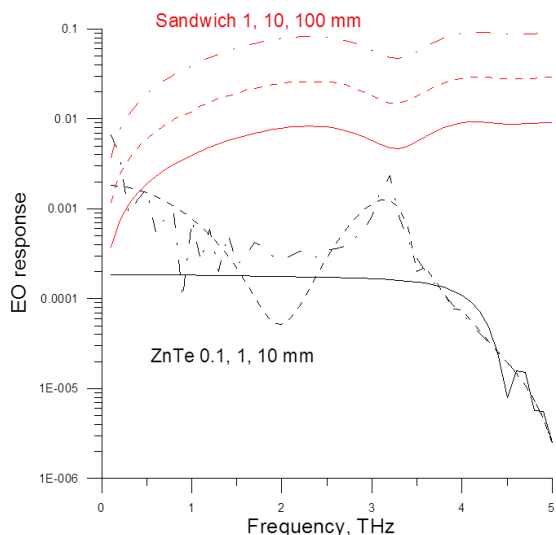
Fig.4. Calculation of the EO response on the same signal of the standard detection technique with the ZnTe crystal and energy detection technique with LN sandwich structure of various lengths (probe beam width 15 μm).

References

1. *Bodrov, S. B., Ilyakov, I. E., Shishkin, B. V., and Stepanov, A. N.* Efficient terahertz generation by optical rectification in Si-LiNbO3-air-metal sandwich structure with variable air gap // Appl. Phys. Lett. 2012. V. 100, N. 20. P. 201114.

2. *Vicario, C., Jazbinsek, M., Ovchinnikov, A. V., Chefonov, O. V., Ashitkov, S. I., Agranat, M. B., and Hauri, C. P.* High efficiency THz generation in DSTMS, DAST and OH1 pumped by Cr:forsterite laser // Opt. Exp. 2015. V. 23. P. 4573-4580.

3. *Wu, Q. and Zhang, X.-C.* Free-space electro-optic sampling of terahertz beams // Appl. Phys. Lett. 1995. V. 67. P. 3523-3525.

4. *Han, P. Y., Tani, M., Pan, F., and Zhang, X.-C.* Use of the organic crystal DAST for terahertz beam applications // Opt. Lett. 2000. V. 25. P. 675-677.

5. *Kitaeva, G. Kh., Kovalev, S. P., Naumova, I. I., Akhmedzhanov, R. A., Ilyakov, I. E., Shishkin, B. V., and Suvorov E. V.* Quasi-phase-matched probe-energy electro-optic sampling as a method of narrowband terahertz detection // Appl. Phys. Lett. 2010. V. 96. P. 071106.

6. *Ilyakov, I. E., Kitaeva, G. Kh., Shishkin, B. V., and Akhmedzhanov, R. A.* Laser pulse amplitude changes induced by terahertz waves under linear electro-optic effect // Appl. Phys. Lett. 2014. V. 104. P. 151107.

7. *Ilyakov, I. E., Kitaeva, G. Kh., Shishkin, B. V., and Akhmedzhanov, R. A.* Terahertz wave electro-optic measurements with optical spectral filtering // Appl. Phys. Lett. 2015. V. 106. P. 121101.

8. *Ilyakov, I. E., Kitaeva, G. Kh., Shishkin, B. V., and Akhmedzhanov, R. A.* Terahertz time-domain electro-optic measurements by femtosecond laser pulses with an edge-cut spectrum // Opt. Lett. 2016. V. 41. P. 2998–3001.

9. *Ilyakov, I.E., Kitaeva, G.Kh., Shishkin, B.V., and Akhmedzhanov, R.A.* Electro-optic sampling of terahertz waves by laser pulses with an edge-cut spectrum in birefringent crystal // Opt. Lett. 2017. V. 42, No. 9. P. 1704–1707.

10. *Ilyakov, I.E., Kitaeva, G.Kh., Shishkin, B.V., and Akhmedzhanov, R.A.* The use of DSTMS crystal for broadband terahertz electro-optic sampling based on laser pulse amplitude changes // Laser Phys. Lett. 2018. V. 15, No. 12. P. 125401.

11. *Bodrov, S. B., Ilyakov, I. E., Shishkin, B. V., and Stepanov, A. N.* Efficient terahertz generation by optical rectification in Si-LiNbO3-air-metal sandwich structure with variable air gap // Appl. Phys. Lett. 2012. V. 100, No. 20. P. 201114.

12. *Tani, M., Kinoshita, T., Nagase, T., Horita, K., Que, C. T., Estacio, E., Yamamoto, K., and Bakunov, M. I.* Non-ellipsometric detection of terahertz radiation using heterodyne EO sampling in the Cherenkov velocity matching scheme // Opt. Exp. 2013. V. 21. P. 9277-9288.

Optical-Terahertz Biphotons

G.Kh. Kitaeva

Lomonosov Moscow State University, Moscow, Russia, gkitaeva@physics.msu.ru

The quantum correlated pairs of photons, usually named as biphotons, are the well known quantum optical objects, comprehensively studied and exploited in modern quantum information schemes [1]. Biphotons are easily generated as pure quantum states in the process of parametric down-conversion (PDC) of optical laser radiation in a quadratic nonlinear medium, and serve further as a basis for preparation of different types of entangled photons and squeezed vacuum states. During PDC each pump photon of frequency ω_p decays into a pair of photons: a signal photon of frequency $\omega_s \geq \omega_p/2$ and an idler photon of lower frequency $\omega_i \leq \omega_p/2$. Formally, only one restriction is imposed on specific values of ω_i and ω_s. It follows from the energy conversation law $\hbar\omega_i + \hbar\omega_s = \hbar\omega_p$, so that the biphotons can be generated in a wide spectral range. Up to now PDC processes are studied mostly in the frequency-degenerate cases, when $\omega_s = \omega_i = \omega_p/2$, or slightly non-degenerate ones, when the difference between signal and idler frequencies is less than the spectral band of optical transmission of the nonlinear medium. We propose to consider properties of biphotons with extremely different frequencies, when the signal photon frequency is just close to ω_p, while the idler photon frequency hits the terahertz range. This regime can be referred as strongly frequency non-degenerate (SFND) PDC.

The SFND regime is interesting with new possibilities that appear in the generation of correlated photons from different spectral ranges, generation of localized long-wave excitations in matter that are bound to optical delocalized states, construction of quantum single-photon sources of terahertz frequencies, quantum calibration of the terahertz wave sources and detectors, and other applications. However, direct transfer of the results and methods, obtained up to now for the PDC in the optical range, to the mixed optical-terahertz case is a quite challenging task. The main problems are caused by the presence of classical thermal field fluctuations at THz frequencies, inherent absorption of the non-linear medium at THz frequencies, and high angular diversity of the generated THz idler photons. Results of the theoretical treatment of correlation functions and frequency-angular distributions of signal and idler photons emitted via spontaneous (low-gain) PDC are presented here accounting the peculiar properties of the SFND regime.

Calculations were made using the nonlinear Kirchhoff law, which expresses the second-order moments of the output PDC-generated fields in terms of the second-order moments of the input fields via elements of the scattering matrix of a nonlinear medi-

um. According to its definition, the scattering matrix $\hat{U}$ consists of coefficients that connect linearly first-order moments of the both signal and idler input and output fields. In particular,

$$\langle a_s^+(L)\rangle = \sum_{s'} U_{ss'}\langle a_{s'}^+(0)\rangle + \sum_{i'} U_{si'}\langle a_{i'}(0)\rangle. \quad (1)$$

Here and below $\langle a_m(z)\rangle$ is considered as an average of the field operator which describes propagation of one plane mode of frequency ω_m ($m = i, s$) along the layer-cut medium at some angle ϑ_m with respect to the layer's normal. The nonlinear Kirchhoff-type law was formulated by D.N. Klyshko within the logic of fluctuation-dissipation approach for parametric light scattering by polaritons [2]. Applying this approach, one does not need to solve exact Heisenberg equations for field operators with the introduction of special noise operators responsible for the absorbing reservoir. It is enough to consider equations for spatially varying *average* values of the field operators. These equations have the same structure as the classical wave equations for slowly varying field amplitudes in an absorptive crystal. They were considered accounting the multi-mode character of the parametric interaction caused by a Gaussian transverse-limited pump beam. Explicit expressions for the multimode scattering matrix elements were obtained for the case of spontaneous PDC.

By substituting the scattering matrix elements into the nonlinear Kirchhoff law the second-order moments of the output fields were obtained. The results show that occupations of output modes $\langle N_m\rangle \equiv \langle a_m^+(L)a_m(L)\rangle$ consist of several different contributions. The first-type contribution (which is true spontaneous) appears due to inherent radiation of the pumped nonlinear medium,

$$\langle N_s^{Spon}\rangle = \kappa_s\left(\sum_i |U_{si}|^2\right) + (\kappa_s - 1)\left(\sum_i |U_{si}|^2\right)\langle N_T\rangle \quad (2)$$

in each signal mode, and

$$\langle N_i^{Spon}\rangle = \left(\sum_s |U_{si}|^2\right) + (1-\kappa_i)\left(\sum_s |U_{si}|^2\right)\langle N_T\rangle + \\ + \left(1 - e^{-2\mu_i L}\right)\langle N_T\rangle \quad (3)$$

in each idler mode. The first terms in Eqs. (2)-(3) contain the pure quantum parts of the nonlinear emission. They are proportional to the sums over all modes of opposite type which make their contributions with the corresponding nonlinear efficiencies $|U_{si}|^2$, whereas

$$U_{si} = iL\gamma_{psi}\, e^{(i\Delta k_\parallel - \mu_i)L/2}\frac{\sinh(i\Delta k_\parallel - \mu_i)L/2}{(i\Delta k_\parallel - \mu_i)L/2}. \quad (4)$$

Here, $\mu_m \equiv \alpha_m / 2\cos\vartheta_m$ depends on the intensity absorption coefficient α_m, $\Delta k_\parallel$ is a longitudinal projection of the wavevector mismatch, and

$$\gamma_{psi} \equiv \frac{2\pi\omega_s\omega_i}{c^2\sqrt{k_{sz}k_{iz}}}E_p\chi^{(2)}$$ is a specific gain per unit

length which depicts efficiency of the parametric interaction between each three plane modes taken at pump, signal and idler frequencies. $\chi^{(2)}$ is an effective value the medium second-order susceptibility. The pump plane mode components are taken with the amplitudes $\quad E_p(\mathbf{k}_p^\perp) \sim w_p^2 \exp(-w_p^2 \mathbf{k}_p^{\perp 2}/4)$ for

transverse wave vectors $\mathbf{k}_p^\perp$; w_p is a Gaussian beam waist. The angular diversity of the idler modes that are parametrically connected with each optical signal mode was analyzed on the basis of Eq. (4). It was shown, that the solid angle occupied by spontaneously emitted idler photons rapidly increases when the idler wave frequency goes down and the idler wave vector becomes comparable with the allowed wave vector mismatch. However, by proper selection of the transverse ($\sim 2w_p$) and longitudinal ($\sim L$) dimensions of the interaction volume, the idler radiation divergence can be kept at a moderate level.

The second terms in expressions for spontaneous emission (2)-(3) are responsible for parametric frequency conversion (in Eq.(2)) or amplification (in Eq.(3)) of classical thermal fluctuations at an idler frequency. They are proportional to the mean number of thermal photons $\langle N_T \rangle = \left[\exp(\hbar\omega_i/k_B T_{cr}) - 1 \right]^{-1}$ at a temperature T_{cr} of the nonlinear medium. The loss-factors κ_s and κ_i account different influence of THz absorption on the efficiencies of parametric processes with thermal and quantum field fluctuations. With a high degree of accuracy they can be taken outside the summation procedures as coefficients that depend only on the THz absorption $\mu_i L$,

$$\kappa_s = 2\left(\mu_i L - 1 + e^{-\mu_i L}\right)/\left(1 - e^{-\mu_i L}\right)^2, \quad \kappa_i = \kappa_s(-\mu_i L). \quad (5)$$

In case of negligibly small absorption the nonlinear contributions of thermal fluctuations to the inherent emission of the medium disappear. The last term in Eq.(3) for the number of emitted idler photons describes the non-parametric thermal radiation by the linear Kirchhoff law.

Apart from the spontaneous emission there can be contributions from the signal or idler radiation incident on the medium. For example, if there is any external idler radiation which is characterized by an effective temperature T_{ext} or with the spectral brightness distributed over all the idler modes with the corresponding mode occupations $\langle N_i \rangle$, the additional photons

$$\langle N_s^{Ind} \rangle = \sum_i |U_{si}|^2 \langle N_i \rangle \qquad (6)$$

are detected at the output in the signal channel. The method of quantum calibration of spectral brightness of an external terahertz radiation is based on comparison between the spontaneous and induced signals [3]. In case of the pure SPDC registration scheme there are no special sources of the external input radiation. However, the equilibrium radiation of the medium environment should be taken into account.

In most cases the temperatures of the medium and of the environment are the same, and a noticeable contribution of external thermal radiation persists only at idler frequencies. As a result, the detected output signal and idler photon numbers are

$$\langle N_s \rangle = \langle N_s^{Spon} \rangle + \langle N_s^{Therm.Ind} \rangle = \kappa_s \left(\langle N_T \rangle + 1 \right) \sum_i |U_{si}|^2,$$
$$\langle N_i \rangle = \langle N_i^{Spon} \rangle + \langle N_i^{Therm.Ind} \rangle = \left(\langle N_T \rangle + 1 \right) \sum_s |U_{si}|^2 + \langle N_T \rangle. \quad (7)$$

Following the nonlinear Kirchhoff law, the second-order moment, which describes correlation of idler and signal fields, is calculated in this case as

$$\langle a_s^+(L)a_i^+(L) \rangle = \left(\langle N_T \rangle + 1 \right) \sum_{s'} U_{is'}U_{ss'} \approx \left(\langle N_T \rangle + 1 \right) U_{is}. \quad (8)$$

In experimental quantum optics the *intensity* correlation function

$$\langle I_s I_i \rangle \sim \left\langle : \sum_s N_s \sum_i N_i : \right\rangle = \sum_{s,i,s',i'} \left\langle a_s^+(L)a_i^+(L)a_{s'}(L)a_{i'}(L) \right\rangle$$

is frequently measured as an indicator of non-classicality of the generated field states. Consider two ideal detectors in signal and idler channels connected by a correlation scheme which measures the normalized intensity correlation function. The readings of such scheme should depend on the nonlinear medium parameters as

$$\frac{\left\langle : \sum_s N_s \sum_i N_i : \right\rangle}{\sum_i \langle N_i \rangle \sum_s \langle N_s \rangle} = 1 + \frac{\left| \sum_{s,i} U_{is} \right|^2}{\kappa_s \sum_{s,i} |U_{is}|^2} \left(\sum_{s,i} |U_{is}|^2 + \sum_i \langle N_T \rangle / \left(\langle N_T \rangle + 1 \right) \right)^{-1}. \quad (9)$$

In the case of properly cooled and transparent medium, low gain and low number of involved modes this ratio is sufficiently more than its classical value 1. However, when absorption, number of modes and the medium temperature are increased, the quantum excess above 1 can become vanishingly small. Final Eq. (9) shows the influence of each of these parameters and can be used as a guide in constructing PDC schemes for generating optical-terahertz biphotons.

References

1. *Bouwmeester D., Ekert A., Zeilinger A.* The Physics of Quantum Information: Quantum Cryptography, Quantum Teleportation, and Quantum Computation // New York: Springer. 2000.

2. *Klyshko, D.N.* Photons and Nonlinear Optics // New York: Gordon and Breach. 1988.

3. *Kitaeva, G. Kh., Penin, A. N., Tuchak, A. N., Shepelev, A.V., Yakunin, P. V.* Measurement of the spectral brightness of terahertz radiation in the process of nonlinear_optical detection // JETP Lett. 2010. V. 92, No. 5, P. 291–294.

Cold-electron bolometer as a photon-noise-limited detector with on-chip electron self-cooling

L.S. Kuzmin[1,2], A.L. Pankratov[1,3], A.V. Gordeeva[1,3], V.O. Zbrozhek[1],

A.V. Blagodatkin[1, 3], L.S. Revin[1, 3]

[1]Nizhny Novgorod State Technical University n.a. R.E. Alekseev, Nizhny Novgorod, Russia
[2]Chalmers University of Technology, Gothenburg, Sweden, leonid.kuzmin@chalmers.se
[3]Institute for Physics of Microstructures of RAS, Nizhny Novgorod, Russia

After discovering the electron cooling by Superconductor-Insulator-Normal metal (SIN) tunnel junctions, significant efforts were applied to obtain an effective on-chip cooler for mm/IR detectors. We have developed a Cold-Electron Bolometer (CEB) with effective direct electron self-cooling of the absorber [1], [2]. A photon-noise-limited pixel, consisting of an array of CEBs with self-cooling, is realized for OLIMPO Balloon Telescope for incoming power P_{in} up to 60 pW at phonon temperature T_{ph} = 310 mK. Operation of the bolometer at electron temperature less than phonon temperature significantly increases its sensitivity so that the noise equivalent power goes beyond the photon-noise-limited mode, which means that the internal bolometer noise is smaller than the noise of incoming signal [3]. We demonstrate the electron cooling from 310 to 120 mK without signal and from 410 to 225 mK for Pin = 60 pW at 350 GHz. The proposed technology is a potential replacement for the high-cost dilution refrigerators for space applications.

The cold electron bolometer is a SINIS structure, integrated in a planar antenna, designed to absorb terahertz radiation at certain frequency. Its SEM image is shown in Fig.1. The normal metal is made of aluminum with suppressed superconductivity, the tunnel barrier is formed by oxidation of aluminum and the superconducting electrodes are made of clean aluminum. All layers are deposited on a Si substrate by method of shadow evaporation. The volume of the normal absorber is just 0.02 μm^3.

A single CEB can absorb up to 0.3-0.5 pW of power before it saturates. In order to fulfill the requirements of high power load for OLIMPO mission, we connected 192 single CEBs in one array. Each bolometer is integrated in a dipole antenna. The array is tuned to have its maximal absorption at 350 GHz. The experiments have shown that the efficiency of absorption for fabricated samples is more than 50%.

The cold electron bolometer is well described by the heat balance equation for normal absorber with resistance R_N:

$$P_{abs} + I^2 R_N + V^2/R_{leak} = 2*P_{COOL} + \sum V(T_e^2 - T_{ph}^2), (1)$$

where I - tunnel current, V - voltage drop across one SIN junction, P_{abs} - absorbed power, R_{leak} - leakage resistance of SIN junctions, P_{COOL} - cooling power of SIN junctions, $\sum$ - electron-phonon constant, V -

volume of the absorber, T_e and T_{ph} are electron and phonon temperatures of the absorber, respectively.
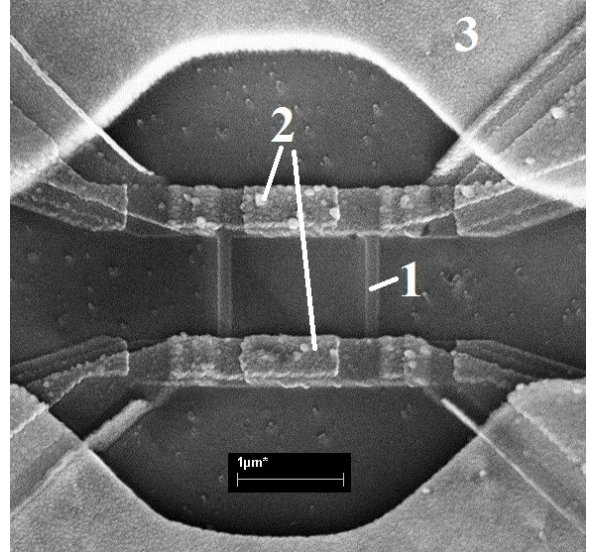

Fig. 1. SEM image of a single cold electron bolometer integrated in a gold dipole antenna. 1 - normal absorber, 2 - SIN junction, 3 - antenna.

The fabricated samples have been cooled in a dilution cryostat down to 310 mK and irradiated by a black body source through a set of quasi-optical filters for 350 GHz. The voltage response and voltage noise at several black body temperatures from 2K to 46 K have been measured, using room temperature ultralow noise amplifiers AD745.

We have compared the experimental IV-curves with Eq. (1) and found that our samples can be fitted very well with the following parameters: critical temperature of superconductor 1.24 K, phonon temperature 310 mK, $\sum$=1.3 nW/K^5/μm^3, normal resistance of SIN junction 1.6 kΩ, R_{leak}=25 MΩ, R_N=50 Ω.

The main characteristic of any detector is the noise equivalent power (NEP). The modern bolometers for astronomical applications are required to have intrinsic NEP less than the photon NEP of incoming signal, i.e. the detector has to be limited by the photon noise. We have shown in a set of our experiments, that we indeed can see the photon noise in our detectors in a broad range of incoming powers from 20 to 60 pW.

The NEP of the bolometer array is shown in Fig.2 for the case of zero incoming power. One can see good agreement between measured and theoretical

values. The optimal operational point of the bolometer can be chosen at the minimal NEP around 12 mV. At this voltage the largest contribution to the bolometer NEP comes from the noise of SIN contacts, which is the sum of shot noise of current through a tunnel junction, noise of heat flow and correlation between them. Next largest NEP component is amplifier NEP. Whereas NEP due to electron-phonon interaction is significantly smaller than other NEP components and can be even disregarded.
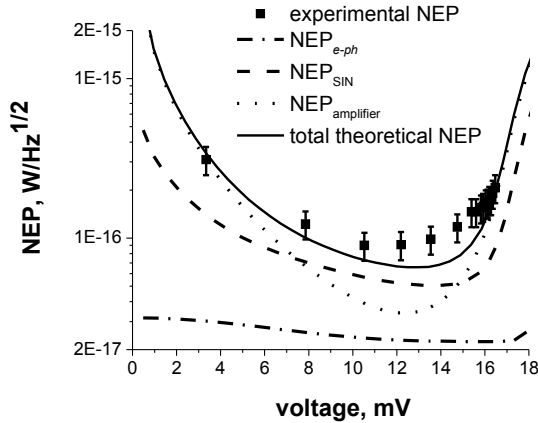

Fig. 2. Noise equivalent power versus voltage on the bolometer array with zero power load. The phonon temperature 310 mK.

In Fig. 3 we show NEP of the same bolometer array but for high power load 60 pW, which corresponds to 32 pW of absorbed power. Now we have one more NEP component - photon noise of absorbed power (straight gray line in Fig. 3). One can see that at voltages 11-12 mV the photon NEP goes a bit higher that all other NEP components together, which means that the detector is photon limited.

Analyzing our data, we found that for black body temperatures above 20 K, the phonon temperature of the sample also increases and can be higher than the cryostat temperature. For example for Fig. 3 the phonon temperature was 380 mK. But even with this overheating the samples show photon limited mode of operation.
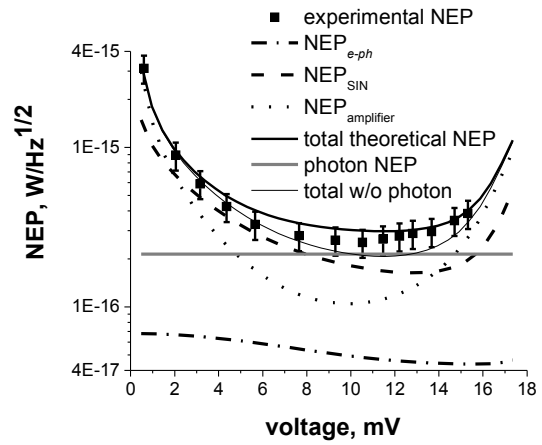
Fig. 3. Noise equivalent power versus voltage on the bolometer array. Radiated power 60 pW. Absorbed power 32 pW.

References

1. *Kuzmin, L.* An Array of Cold-Electron Bolometers with SIN Tunnel Junctions and JFET readout for Cosmology Instruments // Journal of Physics: Conference Series, 8th European Conference on Applied Superconductivity. 2008. V. 97.

2. *Kuzmin, L; Golubev, D.* On the concept of an optimal hot-electron bolometer with NIS tunnel junctions // Physica C-Superconductivity and Its Applications. 2002. V. 372. P. 378-382.

3. *Gordeeva,A.V., et al.* Observation of photon noise by cold-electron bolometers // Appl. Phys. Lett. 2017. V. 110. P. 162603.

Terahertz Time-Domain Spectrometer with Precision Delay Line Encoder

A. A. Mamrashev[1], F. A. Minakov[1,2], L. V. Maximov[1,2], N. A. Nikolaev[1], P. L. Chapovsky[1,2]

[1]Institute of Automation and Electrometry SB RAS, Novosibirsk, Russia, mamrashev@iae.nsk.su
[2]Novosibirsk State University, Novosibirsk, Russia

Introduction

Accuracy of optical delay line is crucial for terahertz time-domain spectroscopy (THz-TDS). Typically such delay line consists of a motorized translation stage with a mounted retroreflector. Random and systematic errors in positioning of the translation stage result in distortion of sampled terahertz pulses and hence terahertz spectra.

It is intuitive that random misplacements in the sampling position (registration jitter) translate into an error in the amplitude of the measured terahertz signal proportional to its derivative. This results in a higher noise floor in the terahertz spectra [1,2]. It was recently found that periodic sampling errors lead to creation of spurious mirror spectra around the error's frequency [3]. In a typical terahertz measurement a series of sampled terahertz pulses or spectra are averaged to achieve better signal to noise ratio. However, even small delays in the sampling start times can actually increase the noise level in the averaged signal [4]. So it was suggested to align terahertz pulses in the time domain before averaging using algorithms from [5].

In the custom-made THz-TDS developed at IA&E SB RAS [6] we used motorized translation stage 8MT173-50-20 (Standa Ltd, Lithuania) with the full movement range of 50 mm (time range of 333 ps) and the step of 1.25 μm (time step of 8.34 fs). In order to independently measure translation stage position in this study we installed an optical encoder Resolute RL32BAT001B50 with RTLA absolute scale (Renishaw, UK) (see Fig. 1). The scale length was 100 mm and its accuracy was 0.5 μm. The encoder resolution was 1 nm. Thus we detected delay line inaccuracies and corrected them.
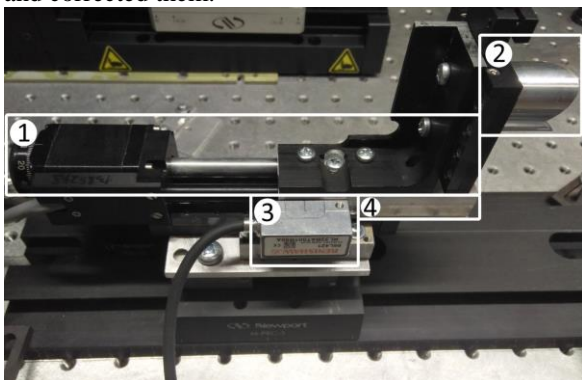
Fig. 1. Upgraded optical delay line consisting of the motorized translation stage (1), the retroreflector (2), the optical encoder (3) and the high accuracy scale (4)

Results

We compared position of the translation stage (L_{st}) with the position measured by the optical encoder (L_{en}). We studied their difference for four translation stages by installing the encoder on each (Fig. 2). It was found that three systematic errors are associated with the measurements: growing offset of the position, periodic error, and drift of the starting position.
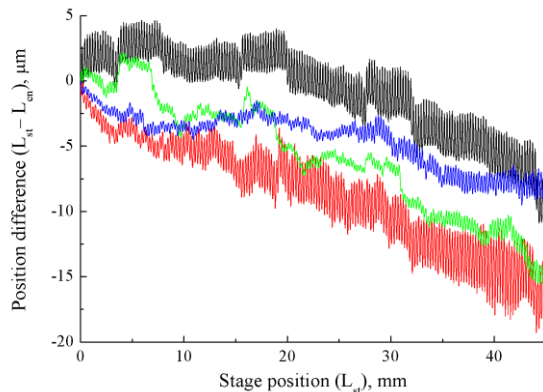

Fig. 2. Difference between the positions of the translation stage (L_{st}) and the optical encoder measurements (L_{en}). The data are presented for four different stages

First, it can be seen from the Fig. 2 that all four translation stages exhibit growing position offset that can roughly be approximated by a linear function. Abrupt changes of the offset may be explained by mechanical defects in the translation stage screw. Total offset varies from –8 to –15 μm for different stages. Such offset manifests itself in a compressed terahertz pulse and consequently stretched terahertz spectrum, i. e. having linearly increasing frequency shift. In our experiments it leads to a total shift of up to 400 MHz at 1 THz. Correction of such systematic error is crucial in the measurements of narrow-band absorption peaks such as spectra of nuclear spin isomers of water vapor [7].

Second, we notice periodic sinusoidal sampling error that becomes apparent after zooming in on the finer structure of the difference between translation stage position and encoder measurements (see Fig. 3).
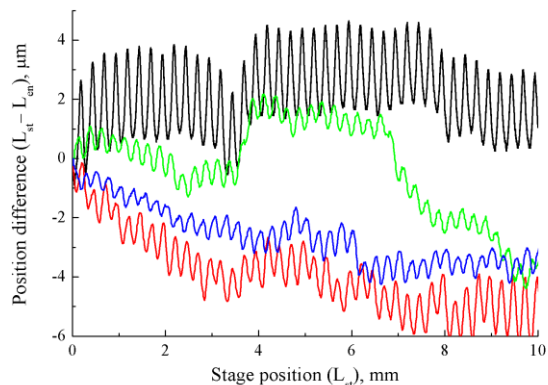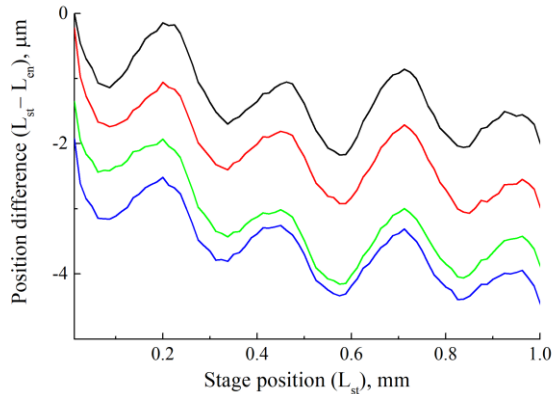

Fig. 3. Difference between the positions of the translation stage (L_{st}) and the optical encoder measurements (L_{en}). The data are presented for four different stages

The period of the oscillations is 250 μm that corresponds well with a single revolution of the stage screw. The amplitude of the oscillation varies from 0.3 to 1.6 μm for different stages. According to [3] such periodic sampling errors result in the presence of additive spurious mirror copies of the main pulse spectrum around error's frequency and its harmonics. In our case oscillation period of 250 μm corresponds to the frequency of 600 GHz. The amplitude of the spurious spectra is proportional to the amplitude of the oscillations. In our measurements it results in the proportionality coefficient as low as 10^{-3} which is comparable with the signal-to-noise ratio making this error difficult to detect.

Fig. 3. Difference between the positions of the translation stage (L_{st}) and the optical encoder measurements (L_{en}). The data are presented for four consecutive measurements of the same translation stage

Finally, we find that the starting position of the same translation stage in the consecutive measurements drifts by less than 1 μm and the drift magnitude gets smaller each time. It results in time delays of the measured terahertz pulses or equivalently in phase shifts in their spectra. This error requires correction before averaging of the series of consecutive terahertz measurements. Otherwise, it may lead to an increased error in the averaged signal.

In conclusion, we found several systematic errors in the optical delay line of THz-TDS by independently measuring its absolute position with precision optical encoder. We found that correction of the position offset of the delay line is crucial in gas analysis. Correction of the starting position drift should be applied before averaging the series of terahertz pulses measured consecutively. Periodic sampling error resulted in a small additive spectral error which can only be found in certain spectra such as ones provided by high contrast band pass filters.

Acknowledgement

References

1. *Jahn D. et al.* On the influence of delay line uncertainty in THz time-domain spectroscopy // Journal of Infrared, Millimeter, and Terahertz Waves. 2016. Vol. 37, No. 6. P. 605–613.

2. *Cohen N. et al.* Experimental signature of registration noise in pulsed terahertz systems // Fluctuation and Noise Letters. 2006. Vol. 6, No. 1. P. L77–L84.

3. *Rehn A. et al.* Periodic sampling errors in terahertz time-domain measurements // Optics Express. 2017. Vol. 25, No. 6. P. 6712.

4. *Humphreys D.A., Naftaly M., Molloy J.F.* Effect of time-delay errors on THz spectroscopy dynamic range // 39th International Conference on Infrared, Millimeter, and Terahertz Waves (IRMMW-THz 2014). IEEE, 2014.

5. *Coakley K.J., Hale P.* Alignment of noisy signals // IEEE Transactions on Instrumentation and Measurement. 2001. Vol. 50, No. 1. P. 141–149.

6. *Antsygin V.D. et al.* Effect of a Magnetic Field on Wideband Terahertz Generation on the Surface of Semiconductors // IEEE Trans. Terahertz Sci. Technol. 2015. Vol. 5, No. 4. P. 673–679.

7. *Mamrashev A.A. et al.* Detection of Nuclear Spin Isomers of Water Molecules by Terahertz Time-Domain Spectroscopy // IEEE Transactions on Terahertz Science and Technology. 2018. Vol. 8, No. 1. P. 13–18.

Temperature dependence of signal spectra generated via spontaneous parametric down-conversion in strongly frequency non-degenerate regime

T.I. Novikova, K.A. Kuznetsov, G.Kh. Kitaeva

MSU Physics Faculty, Moscow, Russia, tanya.novik00@mail.ru

The process of spontaneous parametric down-conversion (SPDC) represents the process of decay of photons of monochromatic radiation (pumping) with a frequency ω_p on pairs of photons due to interaction with quantum fluctuations of the electromagnetic field in a medium with a non-zero quadratic susceptibility $\chi^{(2)}$. As a result, radiation occurred inside the medium, consists of pairs of correlated photons. We propose to consider properties of biphotons with extremely different frequencies, when the signal photon frequency is very close to ω_p, while the idler photon frequency hits the terahertz range. This regime can be referred as strongly frequency non-degenerate parametric down-conversion (SFND PDC). The frequency-angular distributions of the power of signal photons generated in the Stokes and anti-Stokes ranges are measured. We study the dependence of the power of signal photons generated in Stokes and anti-Stokes ranges from the temperature of the non-linear $LiNbO_3$ crystal.
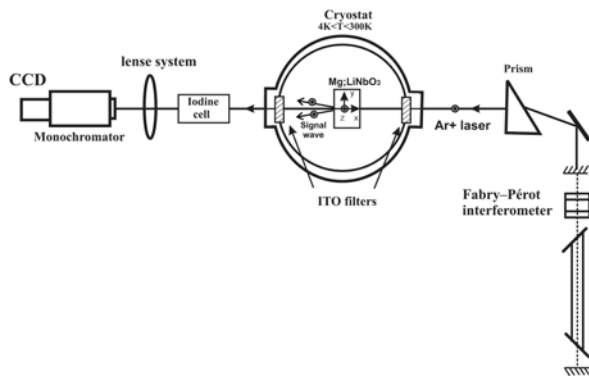
Fig. 1. Experimental setup

In our experiment we use argon laser with generation at a wavelength of 514.5 nm as a pumping source for SPDC. The design of this laser provides the possibility of narrowing the generation line to 100 MHz using the Fabry-Perot interferometer that allow to use narrowband iodine vapor filter for later exclusion of pump radiation. Using the prism we create two beams. One of them allows measuring the pump power without disturbing the main beam, which is a pumping source for 5 mol% MgO-doped $LiNbO_3$ crystal. This crystal is an excellent material for optical frequency converters and it is widely used in quasi-phase-matched conversion applications, because of its large optical nonlinearity. The length of the crystal was L=1.5 cm.

In order to study the influence of thermal fluctuations on the PDC signal the nonlinear crystal has been placed into the cryostat (SCONTEL, Russia) and held at 5 - 300 K. Also, the cryostat in this case has been equipped with a second window for optical pump and signal radiation removal. Stray light from the optical pump was blocked with an iodine cell heated at 75°C. The cryostat windows diameter was D ~ 20 mm. Input and output window of the cryostat were closed by filters, based on indium tin-doped oxide (ITO). They do not allow external thermal terahertz radiation to get into the cryostat. Filters save us from external terahertz thermal photons. We use three lens system in order to focus all signal radiation on the entrance slit of monochromator and get the frequency-angular distributions of emitted photons from CCD camera.

According to the nonlinear Kirchhoff law the power of Stokes and Anti-Stokes radiated photons depends on the crystal temperature in the following way:

$$P_S \sim 1 + <N_T> \qquad (1)$$
$$P_{AS} \sim <N_T> \qquad (2)$$

where $<N_T> = \dfrac{1}{e^{\frac{\hbar\omega}{\kappa T}} - 1}$ - the mean number of thermal photons per mode. So, emitted signal photons in Stokes range arise due to up-conversion of thermal and quantum fluctuations. But anti-Stokes signal photons arise due to up-conversion of thermal fluctuations only. One can see the power of Anti-Stokes photons tends to zero while the temperature tends to zero. During the experiment we cooled the crystal up to 4 K and observed a total disappearance of the Anti-Stokes branch.
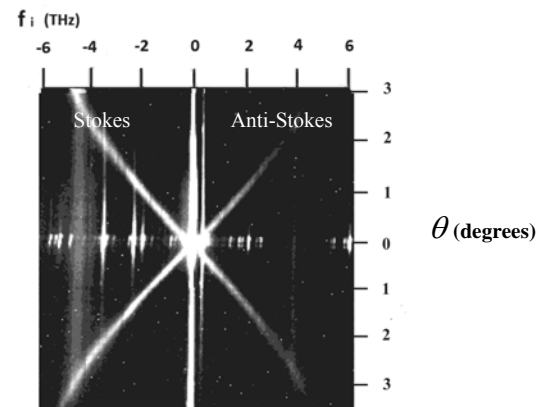

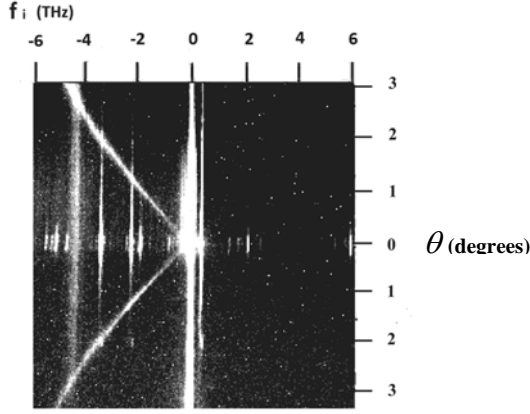**Fig.2.**

Frequency-angular spectrum of PDC at T=297K

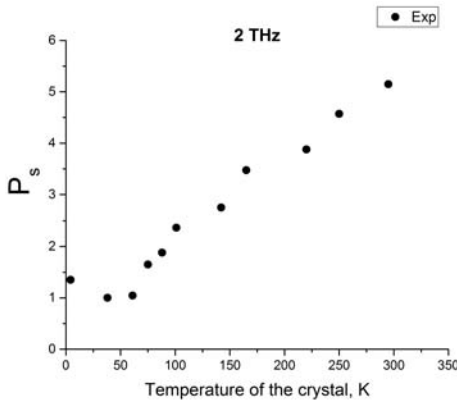**Fig.3.** Frequency-angular spectrum of PDC at T=4K

Fig.4. Experimental data for 2 THz

Using the nonlinear Kirchhoff law, formulated by D.N. Klyshko [1], with account of crystal absorption in the THz idler-frequency range and presence of classical thermal field fluctuations at THz frequencies, it is logical to offer such a theoretical model to describe the obtained results:

$$P_s^{SPDC} = C_{\omega_s}\left(1+\langle N_T \rangle\right)\int S_\omega^{SPDC}(\vartheta_i,\varphi_i)d\vartheta_i d\varphi_i d\vartheta_s d\varphi_s \quad (3)$$

where

$$S_\omega^{SPDC}(\vartheta_i,\varphi_i) = \left(Lw_p\chi^{(2)}\right)^2 \omega_i^3 tg\,\vartheta_i e^{-\frac{w_p^2(\mathbf{k}_{s\perp}+\mathbf{k}_{i\perp})^2}{2}} *$$

$$* \left[\frac{1+\left(i\Delta k_z - \mu_i\right)L - e^{(i\Delta k_z-\mu_i)L}}{\left(\Delta k_z + i\mu_i\right)^2 L^2} + c.c.\right]$$

$$(4)$$

Here, $\mu_m \equiv \alpha_m/2\cos\vartheta_m$ depends on the intensity absorption coefficient α_m, Δk_z is a longitudinal projection of the wave-vector mismatch, w_p is a Gaussian beam waist, L is the length of our crystal, ϑ_i is the angle of idler wave inside the crystal.
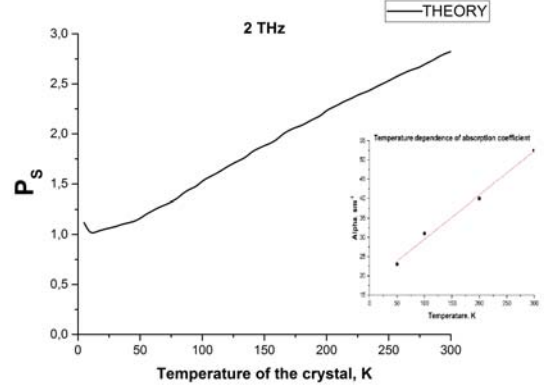
Fig.4. Calculation for 2 THz

The absorption coefficient α_m was taken from the [2]. For crystal absorption in the THz idler-frequency range there were given several values for different temperatures. These data were linearly extrapolated in our calculations. From this extrapolation we took numerical values for our temperatures near 5K. So, considering theoretical values of P_s^{SPDC} we should take into account the approximation error.

References

1. Klyshko D.N. Photons and Nonlinear Optics // New York: Gordon and Breach. 1988.
2. *Xiaojun Wu, Chun Zhou, Wenqian Ronny Huang, Frederike Ahr, and Franz X. Kärtner*. Temperature dependent refractive index and absorption coefficient of congruent lithium niobate crystals in the terahertz range // OPTICS EXPRESS. 2015. V. 23, No.23. P. 29729–29737.

Wideband metamaterial-based array of SINIS bolometers

A.S. Sobolev[1,2], B. Beiranvand[1], A.M. Chekushkin[1,2], A.V. Kudryashov[1], M.A. Tarasov[1,3],
R.A.Yusupov[1,2], A. Gunbina[4], V.F. Vdovin[4], V. Edelman[5]

[1] Moscow Institute for Physics and Technology, Moscow, Russia, sobolev@hitech.cplire.ru
[2] Kotel'nikov Institute of Radio Engineering and Electronics, Moscow, Russia
[3] Chalmers University of Technology, Gothenburg, Sweden
[4] Institute of Applied Physics, N.Novgorod, Russia
[5] Kapitza Institute for Physical Problems RAS

Introduction

Recently we have developed and experimentally studied a wideband 2D-array of periodically arranged electrically small rings, each containing Superconductor-Insulator-Normal metal-Insulator-Superconductor (SINIS) bolometers. Earlier such bolometers in a regular annular antenna array [1] demonstrated voltage responsivity up to 10^9 V/W with a bandwidth of 5-10% in a 350 GHz frequency band. Such detector array can operate in background noise limited condition for incident powers up to 80 pW [2,3]. The typical diameter of the rings was $\lambda/2$, where λ is an effective wavelength on the silicon-vacuum interface related to free-space wavelength λ_0 by

$$\lambda = \frac{\lambda_0}{\sqrt{\frac{\epsilon+1}{2}}} \tag{1}$$

Wavevector **k** of a normally incident plane wave has zero tangential component. For this reason a periodic array with the elementary unit cell size of the order of λ is seen by a normally incident plane wave as a homogeneous thin film with effective impedance Z_{FSS}. The condition of normal incidence is satisfied in quasioptical systems when the detectors array is placed into the focus of a lens where the wase of the Gaussian beam is. Large spatial period of the array reduces the operational frequency bandwidth. In the present work we report on the studies of the wideband array of cold-electron bolometers designed for the range 300-450 GHz and consisting of periodically arranged rings, each containing four bolometers. This periodic array with the unit cell size less than $\lambda/10$ acts as a distributed metamaterial absorber, which is seen as homogeneous metamaterial film by the wave incident at any angle. This fact makes the array applicable for integration into waveguides where all three orthogonal k-vector components of the propagating wave are nonzero. Small unit cell size ensures higher density of bolometers and therefore increases the bandwidth and the dynamic range of a single pixel.

Numerical model and optimization

The chip with a wideband array is designed for mounting on a silicone lens similar to integrated lens antennas. Figure 1 shows a layout of the unit cell with dimension 37um x 38 um in XY plane. A structure made of golden thin film is fabricated on a silicone substrate and the four cold-electron bolometers

are integrated into it. The Floquet ports are placed at the boundaries corresponding to the minimum and the maximum of z-coordinate.
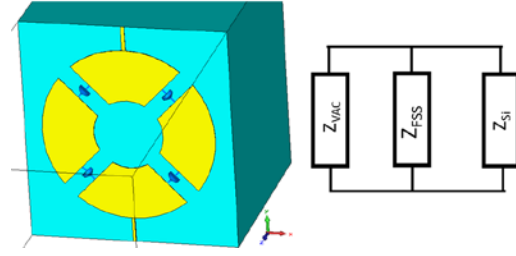

Fig.1. Unit cell design and the lumped elements equivalent schematic

Most of the RF-power coming from the silicone lens is absorbed by the SINIS-bolometers, but some fraction of it is transmitted further into the vacuum half-space because of no backshot. The equivalent microwave schematics of this setup can be represented as a parallel connection of the three lumped impedances: surface impedance Z_{FSS} of the array is shunted by impedance $Z_{VAC} = 377\ \Omega$ and $Z_{SI}=377/\sqrt{11{,}7}\ \Omega$ of vacuum and silicon half-spaces. From this simple schematic one can derive the following formula for the power P_{abs} transmitted from Z_{SI} to Z_{SI}:

$$P_{abs} = \frac{Z_{VAC}}{Z_{FSS}+Z_{VAC}} \cdot \frac{4Z_{SI}Z_{VAC}Z_{FSS}(Z_{FSS}+Z_{VAC})}{(Z_{SI}Z_{FSS}+Z_{SI}Z_{VAC}+Z_{VAC}Z_{FSS})^2} \tag{2}$$

Dependence of P_{abs} as a function of Z_{FSS} is plotted in figure 2. It achieves maximum $P_{abs} = -1$ dB at $Z_{FSS} \approx 80\ \Omega$. This value of Z_{FSS} is slightly less than that of parallel connection of Z_{SI} and Z_{VAC}.
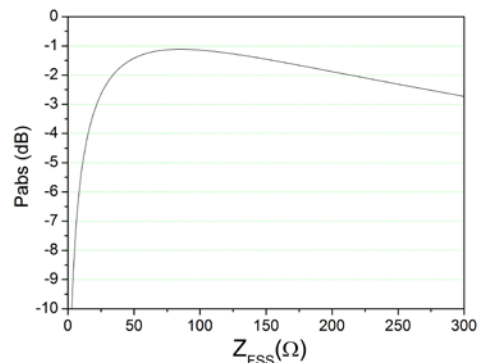

Fig.2. Absorbed power P_{abs} as a function of Z_{FSS}. Maximum P_{abs} corresponds to $Z_{FSS} \approx 80\ \Omega$

During numerical simulations we considered the two lowest port modes with orthogonal polarization and constant distribution of the electric and the magnetic fields. The the E-field of the first Y-polarized mode is directed along the narrow DC-biasing lines that connect adjacent unit cells together and create series inductance, which tunes the capacitance of the SINIS-bolometers out. For the second X-polarized mode Z_{FSS} is determined by the planar capacitance between the rings of the adjacent unit cells.
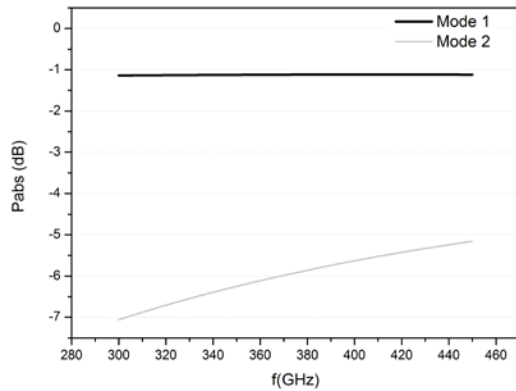

Fig.3. Simulated absorbtion P_{abs} of the SINIS-array fo the two modes with orthogonal polarization

Figure 3 shows the simulated absorbtion of both modes for the array with the optimized unit cell design. and the optimal capacitance C=20 fF and the resistance R=100 Ω of each SINIS-bolometer. According to numerical simulations based on the FDTD-method P_{abs} for the first mode is expected to be close to the -1 dB limit in the whole frequency range 300-450 GHz as like it was predicted by formula (2). The capacitive reactance of the bolometer array seen by the second mode results in much lower P_{abs} ranging from -7 dB to -5 dB.

Experimental test

During experimental tests the spectral response of the sample with the array of SINIS-bolometers was measured in He3 sorption cryostat with optical window and a set of cold neutral density filters that were acting as cold attenuators to reduce the power of room temperature background blackbody radiation. A tuneable external narrowband submm source of radiation was illuminating the 10x10 unit cells array that covered the Airy spot in the focus of the lens. An additional absorber was placed behind the array at some distance from the vacuum side to get rid of the standing waves and make more uniform and wideband frequency response characteristics. The experimentally measured spectral response in the range 240-370 GHz is shown in figure 4. The response is wide and quite nouniform. The nonuniformity may come from the standing waves existing between the cold neutral sensity filters and optical windows. Also the spectral response can be influenced by spurios reflections from some parts of the mesurement setup close by the sample holder.
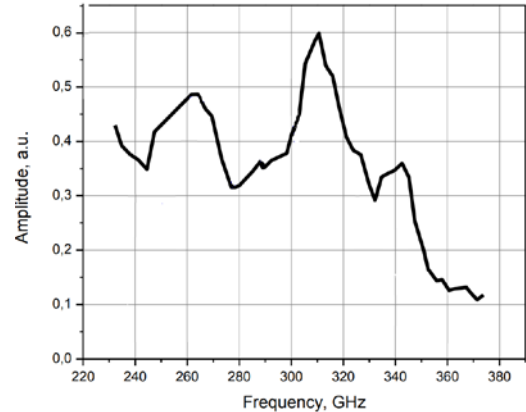

Fig.4. Experimentally measured spectral response of the SINIS-bolometers array

From the measurements with a blackbody source The voltage responsivity of the array with 100 rings measured from a blackbody source was as much as $1.3*10^9$ V/W

References

1. *S.Mahashabde, A.Sobolev, M.Tarasov, G.Tsydanzhapov, L.Kuzmin,* Planar frequency selective bolometric array at 350 GHz // IEEE Trans. Terahertz Sci. and Technol., vol. 5, No 1, pp.37-43, 2015.

2. *Mahashabde, S. Sobolev, A.S., Bengtsson, A.; Andren, D.; Tarasov, M.A.; Salatino, M.; de Bernardis, P.; Masi, S.; Kuzmin, L.S.* A Frequency Selective Surface Based Focal Plane Receiver for the OLIMPO Balloon-Borne Telescope // IEEE Transactions on Terahertz Science and Technology, Volume 5, Issue 1, pp.145-152, 2015

3. *S. Mahashabde, M. A. Tarasov, M. Salatino, A. Sobolev, S. Masi, L. S. Kuzmin,and P. de Bernardis* A distributed-absorber cold-electron bolometer single pixel at 95 GHz // Appl. Phys. Let., 107, 092602, 2015

Arrays of annular cryogenic antennas with SINIS bolometers and cryogenic receivers for SubTHz observatories

M. Tarasov[1], A. Gunbina[2,5], M.Mansfeld[2,5], G. Yakopov[4], A.Chekushkin[1], R. Yusupov[1], S.Lemzyakov[6], V. Edelman[6], and V. Vdovin[2,3,5],

[1]V.Kotelnikov Institute of Radio Engineering an d Electronics RAS
[2]Institute of Applied Physics RAS
[3]P.N. Lebedev Physical Institute of the Russian Academy of Sciences
[4]Special Astrophysical Observatory RAS
[5]Nizhny Novgorod State Technical University n.a. R.E. Alekseev
[6]P.Kapitza Institute for Physical Problems RAS

Series and parallel arrays of annular antennas optimized for 350 GHz frequency band with SINIS (Superconductor - Insulator - Normal metal - Insulator-Superconductor) bolometers and cryogenically cooled receivers for series of modern SubTHz observatories have been designed, fabricated and studied. The detectors are matched to incoming beam by an immersion sapphire lens. In the low background power case a voltage responsivity approaches $1.5*10^9$ V/W corresponding to NEP=10^{-17} W/Hz$^{1/2}$. The current responsivity for parallel array is $4*10^4$ A/W and shot noise limited intrinsic noise equivalent power is NEP=$4*10^{-18}$ W/Hz$^{1/2}$. At the background radiation temperature level of 2.7 K the responsivity to variations of radiation temperature is over 75 µV/K. The intrinsic time constant of the bolometer array is 0.1-0.2 µs.

Introduction

Observation of the CMB radiation anisotropy and some other objects of cold Universe are the priority tasks for ambitious projects in radioastronomy where some new observatories are under development: international space observatory Millimetron, international observatory Suffa (Uzbekistan) and QTT observatory, China. Technical requirements for receivers of listed observatories are rather contradictive, high sensitivity should be combined with a wide dynamic range and a low time constant. Room-temperature semiconducting electronics practically expired potential for improvement and superconducting devices offer promising potential. Only superconductors (TES, KID and other) and cryogenically cooled electronics gives possibility to provide new observatories by proper instruments. A realistic alternative to transition edge sensors (TES) can be SINIS bolometers that provide high responsivity, wide dynamic range and high speed. In present contribution we study performance of such bolometers integrated in series and parallel arrays.

Design and fabrication

Bolometers were integrated in annular ring antennas designed for central frequency of 345 GHz. Antennas were arranged in series and parallel arrays to increase saturation power and dynamic range. The layout of SINIS bolometers was modified to increase the volume of superconducting electrodes up to 100 times (area from 2 µm^2 in our previous designs [1, 2] to 250 µm^2) to reduce overheating by strong dilution of hot quasiparticles in such big volume. Another layout modification is in eliminating of additional layer of so-called thin gold that suppressed superconductivity and connecting Al electrodes directly to thick TiAuPd antennas that also improve cooling of superconducting electrodes.

Measurement setup

Our previous arrangement of experiment was based on a back-to-back horn that reduces a role of antenna dimensions on overall spectral characteristics and beampattern. In present research we have developed results of previous results [1, 2] and used immersion sapphire lens instead of horn. Such substrate lens provides direct illumination of array, avoid substrate modes, and increase the gain of planar antenna. Top view of dilution cryostat [3] with 3 such lenses is presented in Fig. 1. Each sample was connected to room-temperature electronics through cold resistors that provide suppression of interferences and noise. The sapphire hemisphere lens diameter is 8 mm. Total extension for hyperhemisphere should be 1.5 mm, in this case antenna on the chip 0.28 mm thick is placed in the second focus of elliptical lens. Such elliptical lens convert a spherical wave into a planar wave.

Cryogenic fast radiation source comprising NiCr film on sapphire substrate was equipped with a thermometer and placed on 0.5 K temperature stage. Bandpass and lowpass filters between such source and sample determine the bandwidth of irradiating power.
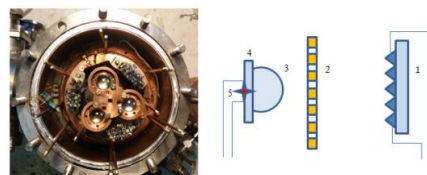

Fig. 1. Photo of opened cryostat with three samples on three sapphire lenses (left), and schematics of sensitivity measurements (right): 1 fast radiation source, 2 bandpass and lowpass filters, 3 hemisphere lens, 4 extension substrate, 5– bolometer array

Experimental results

The asymptotic resistance for single ring is 1700 Ω, for series array of 25 rings it is 39 кΩ, and for 25 parallel rings it is 65 Ω. Responsivity of bolometers was measured by varying the radiation source temperature from initial 0.5 K by applying DC

current through NiCr film on sapphire substrate suspended on thin wires. We compared voltage response of series array for variation of bath temperature and for variation of radiation temperature (see Fig. 2). Dependencies are identic that is a clear proof of thermal mechanism of response contrary to our results with previous generation of samples with lower volume of superconducting electrodes and different geometry of antennas. Position of maximum is slightly shifted from about 1 nA at low radiation power up to about 1.6 nA for higher power. Estimated power level calculated for receiving of single mode.
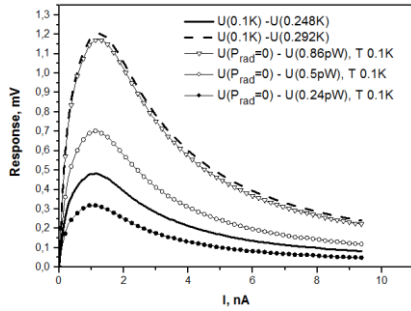
Fig. 2. Voltage response for temperature (0.248 K and 0.292 K) and radiation power

Illustration for saturation and dynamic range is presented in Fig. 3 for series array at bias currents 1 nA and 1.6 nA and for single ring response voltage multiplied by factor of 25 for comparison. Both dependencies can be fitted by a simple relation presented as a line. For radiation power of 2 pW and bias current 1.6 nA the responsivity dV/dP is reduced only by 30% compared to low radiation power case. Small reducing of response for single ring can be due to its position at the edge of chip with lower illumination power. We also compared response of series array for the same signal on the bath temperature (Fig. 4). Three times increase of temperature from 0.1 to 0.3 K leads to decrease of maximum response only by a factor of 1.5. A figure of merit for astronomic applications is radiation temperature responsivity (Fig. 5). At the background power level of 2.7 K the responsivity to variations of radiation temperature is over 75 μV/K. For amplifier noise limited case of 7 nV/Hz$^{1/2}$, the detection of relative radiation temperature variation is at the level of $4*10^{-5}$.
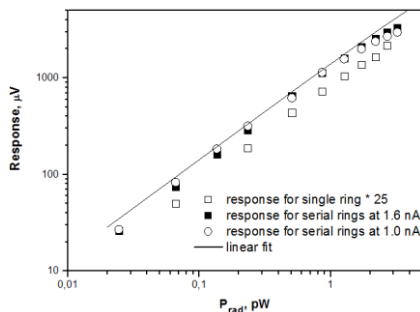

Fig. 3. Response at 0.1 K for series array of 24 rings, single ring x25, and linear fitting

The time constant of such detector (Fig. 6) have been measured by response for the heating pulses of 85 V amplitude and duration of 1 μs. Fitting by exponent of signal increase after the end of heating

pulse shows that the overall time constant of receiver is $\tau_{sum} \approx 0.55$ μs. The main impact to this time constant is due to the readout amplifier that is $\tau_{amp} \approx 0.4$ μs measured separately with test signal from optocoupler pair. From these data we can estimate the intrinsic time constant of the bolometer as 0.1-0.2 μs.
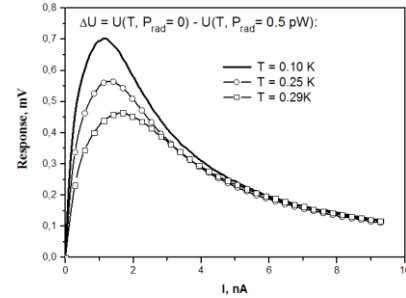

Fig. 4. Response of 25 series array for the same radiation power of 0.5 pW measured at bath temperatures 0.1 K, 0.25 K, and 0.29 K
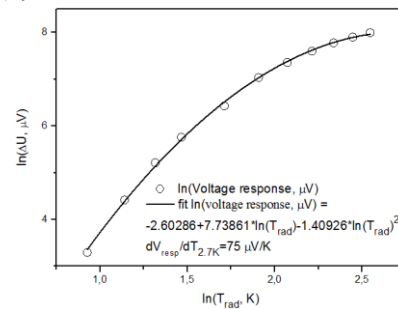

Fig. 5. Logarithmic plot of voltage response for series array at 0.1 K. Radiation temperature responsivity is 75 μV/K at background temperature of 2.7 K
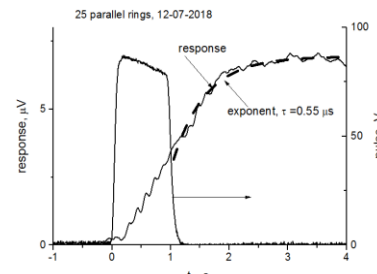

Fig. 6. Probing pulse applied to radiation source (right axis), and output voltage response (left axis) together with fitting by exponent (dashed)

References

1. *S. Mahashabde, A. Sobolev, A. Bengtsson, et al*. A frequency selective surface based focal plane receiver for the OLIMPO balloon-borne telescope //IEEE Trans. on Terahertz Science and Technology. 2015.V.5,N1. P.145.
2. *S. Mahashabde, A. Sobolev, M. Tarasov, et al*. Planar frequency selective bolometric array at 350 GHz //IEEE Trans. on TST. 2015.V.5, No 1. P. 37-43.
3. *V.S. Edelman*. A dilution microcryostat-insert //Instrum. and Exp. Tech. 2009. V. 52, No 2. P. 301-307.
4. *G.M. Rebeiz*. Millimeter-wave and Terahertz integrated circuit antennas // Proc. of the IEEE. 1992. V. 80, No 11, P. 1748-1770

Acknowledgements

26

Technology for NbN HEB based multipixel matrix of THz range

Ivan Tretyakov[1], N. Kaurova[1], S. Raybchun[1] and G.N. Goltsman[1]

[1]Department of Physics, Moscow State University of Education, 29 Malaya Pirogovskaya St, Moscow, 119435, Russia

Abstract—**The influence of homogeneity disorder degree of the thin superconducting NbN film across of Si wafer on characteristics of the Hot Electron Bolometers (HEB) has been investigated. Our experiments have been carried out near the superconducting transition and far below it. The high homogeneity disorder degree of the NbN film has been achieved by preparing the Si substrate surface. The fabricated HEBs all have almost identical R (T) characteristics with a dispersion of Tc and the normal resistance R_{300} of not more than 0.15K and 2 Ω, respectively. The quality of the devises allows us to demonstrate clearly the influence of non-equilibrium processes in the S'SS' system on the device performance. Our fabrication technology also allows creating multiplex heterodyne and direct detector matrices based the HEB devices.**

[1] INTRODUCTION

The disordered thin superconducting NbN film has found an application as a sensitive element in bolometric detectors of terahertz and infrared ranges, such as HEB devices [1], single-photon SSPD detectors [2]. Modern instruments of observational astronomy SOFIA [3] and GUSTO [4] require the use of matrix detectors for the terahertz range. Each pixel of the matrix – an HEB - is now considered as a separate detector, requiring individual adjustment of the bias voltage and local oscillator (LO) power. With the matrix size of several dozen pixels, this approach is impractical from the point of view of Allan's time. A solution to the problem can become unified and not requiring individual adjustment HEB pixels. Modern HEBs as heterodyne detectors have practically reached their sensitivity limit [5,6]. However, the task of fabricating a relatively large number of similar HEBs remains unresolved. In this paper, we present the capabilities of our technology of NbN HEB fabricating on Si substrates that allows us to obtain detectors with very close R (T) characteristics for geometrically identical detectors within one batch. The key aspects of our technology are the surface preparing process of the high-resistance Si substrate, as well as the process of cleaning the NbN contact areas before the Au deposition.

[2] RESULTS

For our experiments the NbN film is deposited by the AJA ORION 8 unit for 69 sec. to achieve a thickness of 5 nm. Fig. 1 shows a schematic of the HEB. The detector consists of a superconducting NbN film embedded into Ti/Au terminals of a planar antenna deposited onto a Si substrate. The detector inner part consists of an NbN film between the antenna inner terminals, the so called NbN bridge with a given width W and length L, and a multilayer structure of the NbN/Ti/Au antenna –outer terminals. The multilayer NbN/Ti/Au has a critical temperature Tc2 lower than the Tc1 of the NbN bridge.
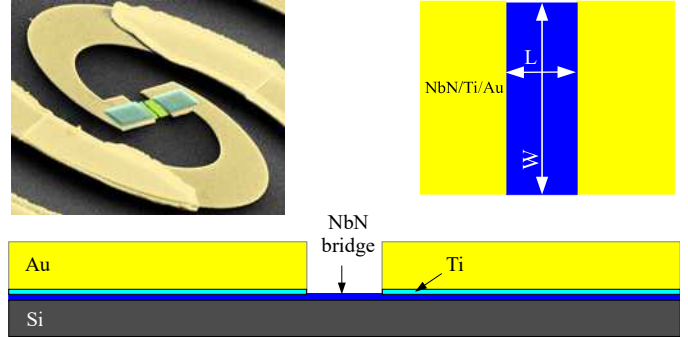

Fig. 1. A schematic diagram of the HEB.

The cleaning process of the Si substrate surface allows us to fabricate devices with a Tc1 deviation not more than 0.1K, for example, the *in-situ* technology presented in [7] gives a Tc1 dispersion of about 0,7-0,8 K. Fig. 2 presents a family of R (T) characteristics of NbN HEBs. The similar shape of the R (T) curves demonstrates HEBs fabricated within *in-situ* NbN/Au technology for HEB contacts [6]. The similarity of the Tc1 for the fabricated NbN HEBs across Si wafer gives the possibility to operate them at one common physical temperature as a single direct detector, or as a heterodyne detector with the same local oscillator power.
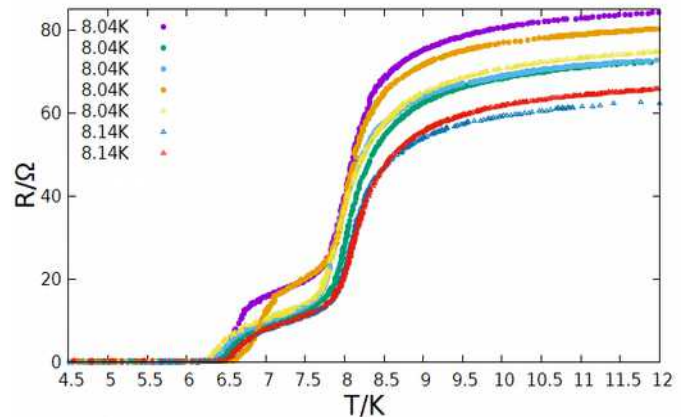

Fig. 2. A family of R (T) characteristics of the NbN HEBs.

The NbN film under Ti/Au antenna ports was cleaned in Ar and O2 plasmas. The idea of cleaning was first proposed and applied for HEBs in [5]. This process made it possible to minimize the contact resistance between NbN and Ti/Au, and also to reduce the dispersion of the normal resistances to not more than 2 Ω for detectors with the same L/W ratio. The quality of the electrical contact between NbN and Ti/Au explains the appearance of second transition on R (T) due to proximity effect. The HEBs resistance at Tc1<T<Tc2 is built into the NbN superconducting bridge and is caused by the conversion of the normal electron current to the current of Cooper pairs over a length of oder ξ [7]. Moreover, the charge conversion process also could influence the coordinate

dependence of the energy gap near Tc1 [8]. It leads to a smearing of the superconducting transition and an increase of ΔTc1.

Fig. 3 shows a family of the IV curves of detector 1498_2 # 9 taken at the bath temperature ranging from 5 K to T>Tc1. Fig. 3 we interpret as the evolution of the HEB IV curves upon transition from the S'SS' state [8], when the NbN bridge and the multilayer NbN/Ti/Au are in the superconducting state to the NSN [8] state where the NbN bridge is superconducting but multilayer NbN/Ti/Au is in the normal state.
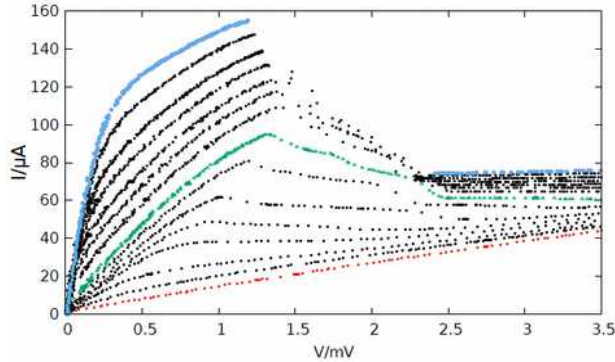
Fig. 3. A family of IV curves of detector 1498_2 # 9 in the temperature range from 5 K to T> Tc1.

An HEB as a direct detector of THz radiation operates at the edge of the superconducting transition, being in the NSN state. In the mixer mode, an HEB operates at T<<Tc1, being in the S'SS' state. The deviation in the measured minimal NEP of our HEB detectors is less than 15% at level of $5*10^{-13}$ W/√Hz. The dispersion of the HEBs optimal bias current and voltage is 3-5 μA and 0.1 mV respectively. Such a small dispersion also indicates the identity of the HEBs. The measured values of the NEP are worse than the calculated value $1-2*10^{-14}$ W/√Hz, which can be attributed to the influence of the processes at the metal/superconductor interface, which reduce the dR/dT of the detector and give an additional contribution to the detector noise.

Fig. 4 presents the results of our study of HEB detectors as mixers in the S'SS' state. These mixers were fabricated using *in-situ* technology [6]. However, the surface of the Si substrate was not prepared in a special way before NbN deposition. The L/W bridge ratio was kept constant at 0.1-0.12 for all devices. Fig. 4 presents the dependence of the HEB noise temperature Tn measured at 2.5THz on the width of the NbN bridge. As can be seen from Fig. 4, there is a certain optimum volume of the NbN bridge with a minimum dispersion and a minimum Tn of 650K. The dispersion of Tn for devices with the same L and W fabricated from the same NbN film clearly demonstrates the influence of homogeneity disorder degree of the thin superconducting NbN film across of Si wafer on the characteristics of final devices. The optimal W indicates some optimal ratio of the NbN bridge heat capacity C, the resistance coordinate dependences ρ(L) and the distribution of the order parameter Δ(L) presented in Fig. 20a of [9]. For large W the optimal value the volume of the NbN bridge increases also as its C, and accordingly the voltage responsivity Sv falls. The decrease of W of the NbN bridge leads to a proportional decrease of the ρ(L) and the "hump" Δ(L) widths in Fig. 20a of [9].
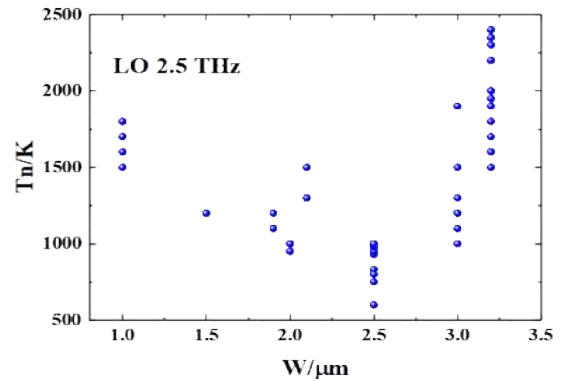

Fig. 4. The noise temperature Tn of an HEB bolometer as function of the width of the its superconducting NbN bridge.

Since, the absolute value of the "hump" Δ(L) width decreases, taking into account the diffusion length Le for a thin film of NbN in the resistive state [6, 10], some electrons absorbing the signal power, can escape into metal contacts not through the Andreev reflection but through tunneling, carrying energy with them - without a contribution to the deviation ρ(L) and the the voltage responsivity of the entire system will fall.

[3] CONCLUSION

We demonstrated a fabrication technology of NbN HEB on Si substrates which allows us to obtain detectors with almost identical R (T) characteristics and explain the optimal dimensions of the bridge for a low Tn. This technology allows the simple creating of the multiplex heterodyne and direct detector matrix based on HEB devices.

ACKNOWLEDGEMENTS

REFERENCES

[1] E. M. Gershenzon, G. N. Goltsman, I. G. Gogidze, Y. P. Gusev, A. I. Elantiev, B. S. Karasik, and A. D. Semenov, "Millimeter and submillimeter range mixer based on electronic heating of superconducting films in the resistive state," Superconductivity, vol. 3, no. 10, pp. 1582–1597, 1990

[2] A. Semenov, G. N. Gol'tsman, R. Sobolewski, "Hot-Electron Effect in Superconductors and Its Applications for Radiation Sensors", LLE Review, V 87, pp 134-152, 2002.

[3] www.sofia.usra.edu

[4] www.sron.nl/missions-astrophysics/gusto

[5] J. J. A. Baselmans, M. Hajenius, J. R. Gao, T. M. Klapwijk, P. A. J. de Korte, B. Voronov, and G. Gol'tsman, "Doubling of sensitivity and bandwidth in phonon cooled hot electron bolometer mixers," Appl. Phys. Lett., vol. 84, pp. 1958–1960, 2004.

[6] I. Tretyakov, S. Ryabchun, M. Finkel, A. Maslennikova, N. Kaurova, A. Lobastova, B. Voronov, and G. Goltsman, "Low noise and wide bandwidth of NbN hot-electron bolometer mixers," Appl. Phys. Lett., vol. 98, p. 033507, 2011.

[7] M. Shcherbatenko, I. Tretyakov, Y. Lobanov, S. N. Maslennikov, N. Kaurova, M. Finkel, B. Voronov, G. Goltsman, and T. M. Klapwijk, "Nonequilibrium interpretation of DC properties of NbN superconducting hot electron bolometers," Appl. Phys. Lett., vol. 109, p. 132602, 2016.

[8] N. Vercruyssen, T.G.A. Verhagen, M.G. Flokstra, J.P. Pekola, and T.M. Klapwijk, Phys.Rev. B85, 224503, 2012.

[9] T. M. Klapwijk and A. V. Semenov, "Engineering Physics of Superconducting Hot-Electron Bolometer Mixers," IEEE Transactions on Terahertz Science and Technology, vol/ 7, issue 6, pp. 627 - 648, 2017.

[10] A.D. Semenov, G.N. Goltsman, and A.A. Korneev, Physica C 351, 349, 2001.

Response of carbon nanotube film transistor to the THz radiation

V. V. Belosevich[1], I. A. Gayduchenko[2], N. A. Titova[2], E. S. Zhukova[1], G. N. Goltsman[2], G. E. Fedorov[1]

[1]Moscow Institute of Physics and Technology, Moscow, Russia, vsevolod.belosevich@phystech.edu
[2]Moscow State Pedagogical University, Moscow, Russia

Nowadays radiation in teraherz frequency range has many applications in different areas of science and industry. Despite years of research, the THz region of electromagnetic spectrum still has lack of sources and detectors. Almost all created high sensitive detectors require cooling to liquid nitrogen or even helium temperatures.

In 1996 M.Dyakonov and M.Shur have shown theoretically [1] that a short channel High Electron Mobility Transistor demonstrate a resonance response to electromagnetic radiation at the plasma oscillation frequencies of the two-dimensional electrons in the device. The described device implements Field-Effect-Transistor (FET) configuration and consists of transport channel framed by two contacts (source and drain) and a top-gate contact. As a consequence of the high plasma wave velocity and small FET dimensions, the plasma wave frequencies are in the terahertz range. The plasma waves are accompanied by a variation of a dipole moment created by charges in the FET channel and the mirror image charges in the gate.

In that view devices based on carbon nanostructures look promising because of operation with zero bias and their high electron drift mobility. In carbon nanonutubes (CNT) it reaches 100'000cm2/Vs [2].
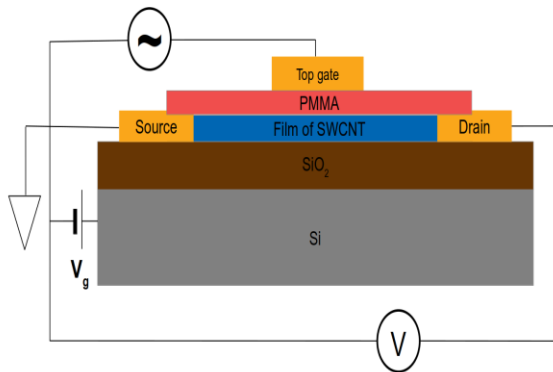

Fig. 1. Scheme of internal structure of the sample

In this work we report on first studies of efficiency of such detectors (Fig.1). Using CVD method we grew our CNT films on oxidized silicon substrate that serves as a back gate of the transistor. After that using photo- and electron- lithography we made Ti/Au contacts and put over a layer of overexposed PMMA resist as dielectric [3]. On the top of the PMMA we plated one more contact as top-gate. Source contact and top gate are part of a broadband log-spiral antenna that couple the radiation (see figure 1). Applying back gate voltage we control concentration and type of charge carriers in transport channel. We observed a strong photoresponse in a broad spectral range from 130 to 900GHz.

In order to charecterize the device we first sweep potential of bottom gate and measure conductance as a function of the back gate voltage applying source-drain voltage of 10meV (see Figure 2). All measurements were carried out at three temperatures (room temperature, temperature of liquid nitrogen, temperature of liquid helium). We further used these dependencies to calculate Seeback coefficient and compare its dependence on Vg to the gate dependence of the device responsivity (see figure 4).
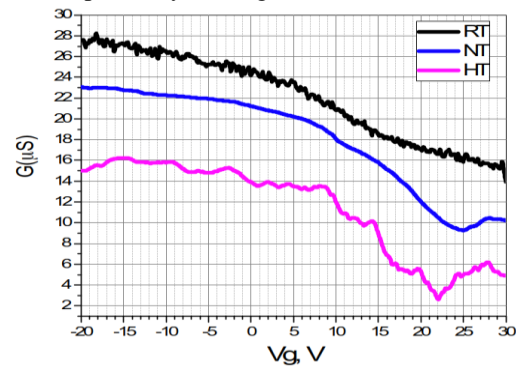

Fig. 2. Transistor characteristic of the tested sample measured at three temperatures (300K, 77K, 8K)

As seen from the figure 2 the conductance decreases with cooling down, This indicates that there are more semiconducting tubes in the film than metallic, which corresponds with the probabilistic estimate obtained from the conditions on the chirality vector components. [4]

At the lowest temperature on figure 2 (8 K) it is possible to observe numerous irregularities. This happens due to different reasons but poor dielectric quality that introduces lots of local potential fluctuations makes this pattern non-reproducible. Charge traps formed by organic molecules of PMMA make noise during the low-temperature experiment.
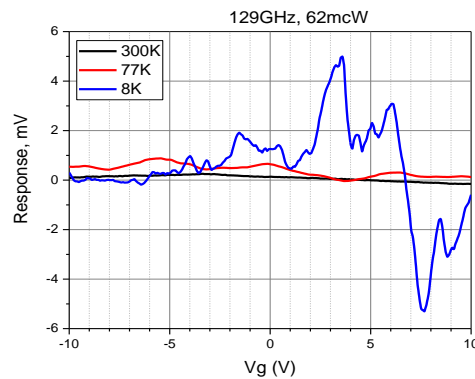

Fig. 3. The photoresponse of the device to 129GHz radiation at three temperatures (300K, 77K, 8K)

29

The experimental curves of photoreponse to different temperatures are shown on figure 3. It can be seen that the response grows up with cooling down the device. On the figure 4 responsivity curves are shown. As can be seen from the figure 4 all curves have a common trend regardless to the frequency of radiation. The main mechanism involved in rectifying the THz radiation was identified.
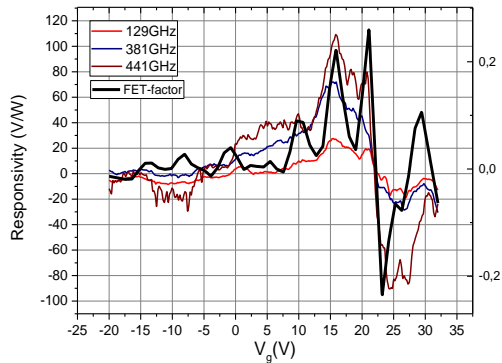

Fig. 4. The responsivity of the device to different frequencies radiation at liquid helium temperature

Thus, we showed that FET device with carbon nanotube film as a transport channel detect THz radiation in all temperature ranges. Previously CVD graphene device in the Dyakonov-Shur configuration was shown to have 1V/W responsivity [5] and graphene encapsulated between

two slabs of hexagonal boron nitride 20V/W [6]. In comparison with this CNT device shows responsivity up to 100V/W to radiation of THz frequency range. This fact makes CNT devices promising for industry and interesting for scientific research.

References

1. *Dyakonov, M. I., Shur, M. S.* Detection, mixing, and frequency multiplication of terahertz radiation by two-dimensional electronic fluid // IEEE Transactions on Electron Devices 1996. V. 43. P. 380–387.

2. *Dürkop T.,Getty S. A. ,Cobas Enrique, and Fuhrer M. S.* Extraordinary Mobility in Semiconducting Carbon Nanotubes // *Nano Letters* 2004 *4* (1), 35-39

3. *Sanne A., Movva H. C. P., Kang S., McClellan C., Corbet C. M., Banerjee S. K.* Poly(methyl methacrylate) as a self-assembled gate dielectric for graphene field-effect transistors // Appl. Phys. Lett 2014. 104 (8), 83106.

4. *Charlier J. C. , Blase X., Roche S.* Electronic and transport properties of nanotubes // B: Reviews of Modern Physics 2007. V.79 Iss 2.

5. *Fedorov G.E. , Gaiduchenko I.A., Golikov A.D., Obraztsova E.D., Rybin M.G., Voronov B.M., Coquillat D., Diakonova N., Knap W., Goltsman G.N.* Response of Graphene Based Gated Nanodevices Exposed to THz Radiation // EPJ Web of Conferences 103, 10003 (2015).

6. *Bandurin D.A., Gaiduchenko I.A., Cao Y., Moskotin M., Principi A., Grigorieva I.V., Goltsman G.N., Fedorov G.E., Svintsov D.* Dual origin of room temperature sub-terahertz photoresponse in graphene field effect transistors // Applied Physics Letters 112, 141101 (2018).

Spectral measurements of THz radiation
emitted from intrinsic Josephson junction stacks

V.P. Koshelets[1], N.V. Kinev[1], A.B. Ermakov[1], F. Rudau[2], R. Wieland[2], D. Koelle[2], R. Kleiner[2], and H.B. Wang[3]

[1] Kotel'nikov Institute of Radio Engineering and Electronics RAS, Moscow 125009, Russia; valery@hitech.cplire.ru
[2] Physikalisches Institut and Center for Collective Quantum Phenomena in LISA+, Universität Tübingen, D-72076 Tübingen, Germany;
[3] Research Institute of Superconductor Electronics, Nanjing University, Nanjing 210093, China.

A superconducting integrated receiver (SIR) comprises all of the elements needed for heterodyne detection on a single chip. Recently, the SIR was successfully implemented for the first spectral measurements of terahertz (THz) radiation emitted from intrinsic Josephson junction stacks (BSCCO mesa) at frequencies up to 750 GHz; a linewidth below 10 MHz has been recorded in the high bias regime. In this report the results of the spectral measurements of THz radiation emitted from intrinsic Josephson junction stacks are summarized; recent results of spectrometric gas detection using THz radiation from a BSCCO mesa are presented.

In recent years, coherent THz emission has been obtained from stacks of intrinsic Josephson junctions (IJJs), created naturally in the BSCCO unit cell with the CuO layers forming the superconducting electrodes and the BiO and SrO layers forming the barrier layer [1, 2]; a 1- µm-thick crystal consists of about 670 IJJs. Terahertz emission from BSCCO mesa has been obtained both at a low bias (where the temperature distribution in the stack is almost homogeneous) and a high bias regime (where an over-heated part and a cold part of the sample coexist) [3, 4].

Coherent emission above 1 THz by intrinsic Josephson BSCCO junction stacks with improved cooling has been demonstrated [5, 6]. Due to the variable size of the hot spot and the temperature rise caused by the self-heating, the emission frequency can be tuned over a wide range of up to 700 GHz [5]. So far, emitted by one device power up to 30 µW was obtained [7, 8]. These are very encouraging results, although for most practical application spectral properties of the novel oscillators are vitally important.

The spectral characteristics of the oscillator were studied using the high-sensitivity super-heterodyne SIR, which was developed at Kotel'nikov IREE [9 - 12]. Such a receiver is intended to perform spectral studies of the electromagnetic radiation in the frequency range 450–700 GHz and successfully used for measuring the profiles of the spectral lines of the gas-molecule radiation and absorption and for the spectral study of any external terahertz oscillator radiating in the operation frequency range of the receiver. The best noise temperature of the SIR is 120 K and its spectral resolution is better than 0.1 MHz, which exceeds the resolution of modern terahertz-range Fourier spectrometers by several orders of magnitude.

Two configurations for the oscillator and receiver location were used: in the first case the oscillator was located in a cryostat of the SIR in the vicinity of the mixing unit [11]; in the second case the oscillator and the receiver were located in independent cryostats with Mylar quasioptical windows. The SIR operates at temperature of about 4.5 K, whereas the optimal BSCCO-oscillator temperature is 20–50 K. The spectral lines of the oscillator radiation are recorded by the SIR and displayed on the spectrum-analyzer screen in the intermediate-frequency range 4–8 GHz. The spectrum analyzer allows one to average the signal, read it by a computer, and perform other necessary digital operations for the spectrum analysis and processing.

Application of the SIR has allowed to measure radiation emitted from intrinsic Josephson junction stacks in both regimes with spectral resolution better than 1 MHz [4].While at low bias we found that linewidth is not smaller than 500 MHz, at high bias, emission linewidth turned out to be in the range 10–100 MHz (see Fig. 1a). We attribute this to the hot spot acting as a synchronizing element; a linewidth as narrow as 7 MHz has been recorded at high bias [12], see Fig. 1b.
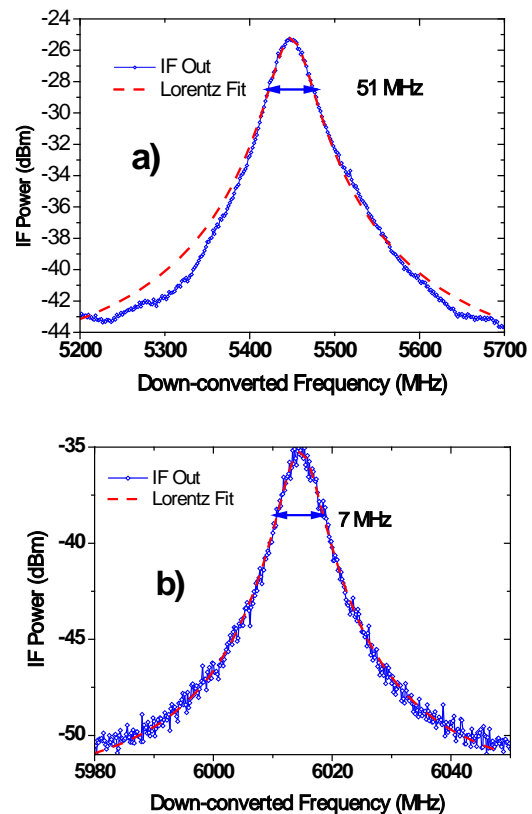

Fig. 1. Down-converted spectrum of the BSCCO at 527 (a) 476 GHz (b) in the high bias regime; dashed line is a Lorenzian fit with full linewidth 51 and 7 MHz respectively.

Typical dependencies of the linewidth on the BSCCO frequency both in the low-bias and high-bias regimes that were measured by the SIR are presented in the Fig. 2. Important to note that the tuning of the BSCCO oscillator frequency is continuous over the range; that was confirmed by fine tuning of the SIR LO frequency. Actually for the presented data the lowest measured frequency of about 550 GHz was limited by the BSCCO mesa, while losses in the Nb interconnection lines of the SIR restrict the measurements at frequencies higher than 730 GHz.
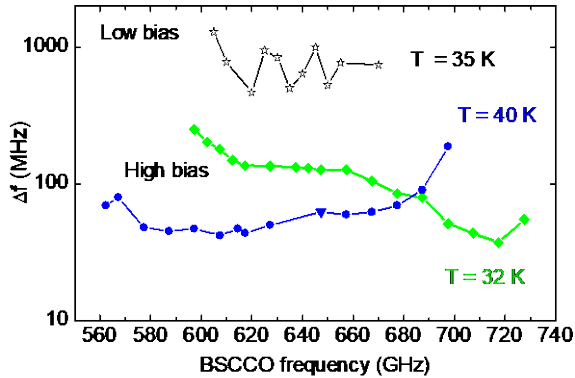
Fig. 2. Typical dependence of the BSCCO linewidth on the frequency (measured for the different sample temperatures — solid (open) symbols are for high (low) bias regime.

A combination of the BSCCO mesa and the SIR was used to accurately measure the terahertz absorption spectra of ammonia and water vapor [13]. In this experiment, the bias current through the BSCCO emitter is kept at a constant value, tuned to the respective gas-line frequency, and intermediate-frequency (IF) spectra are taken using the SIR.
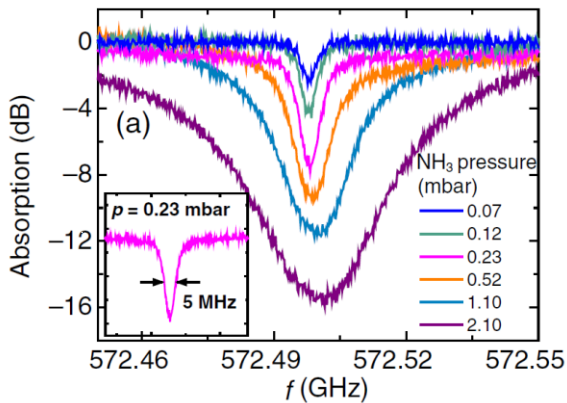

Fig. 3. Terahertz absorption spectra of ammonia (mixed with water; 10% solution) at different pressures by a BSCCO emitter and a SIR terahertz detector. The emitter and the SIR are operated at T_b = 4.2 K. The empty cell curve is subtracted from the data. Spectrum of ammonia vapor at p = 0.23 mbar, with an absorption linewidth of 5 MHz is presented as an inset.

Measurements are done at T_b = 4.2 K, where the linewidth of radiation of the emitter is 60 MHz at 572.5 GHz (NH_3). With this setup, high resolution THz absorption spectra of ammonia achieved in a narrow frequency band lower than the linewidth of the BSCCO emitter; see Fig. 3 [13]. The emitter, operated in a free-running mode, is stable enough to permit this kind of measurement. The absorption lines of ammonia are highly broadened at large gas pressures, with the linewidth decreasing with decreasing pressure. For ammonia, at p = 0.23 mbar, which is the order of the concentration of trace gases, a clear absorption dip with an absorption linewidth of about 5 MHz is observed, as shown in the inset of Fig. 3. At p = 0.07 mbar, the measured linewidth is 4 MHz (although affected by Doppler broadening). The observed rotation frequencies of ammonia (572.498 GHz) coincide with literature values. Further improvement of the lowest resolvable linewidth is possible by using proper feedback techniques for the oscillator [10].

References

1. *Kleiner, R., Muller, P., Kunkell, G., Steinmeyer, F.* Intrinsic Josephson effects in Bi Sr CaCu O single crystals // Phys. Rev.Lett. 1992. V. 68, P. 2394–2397.

2. *Ozyuzer, L., et al.* Emission of coherent THz radiation from superconductors,"Science, 2007. V. 318, No. 5854. P. 1291–1293.

3. *Wang, H. B., et al.* Coherent terahertz emission of intrinsic Josephson junction stacks in the hot spot regime // Phys. Rev. Lett. 2010. V. 105, No. 5. Art. ID 057002.

4. *Li, M. Y., et al.* Linewidth dependence of coherent terahertz emission from BiSrCaCuO intrinsic Josephson junction stacks in the hotspot regime // 2012. Phys. Rev. B. V. 86. Art. ID 060505.

5. *Ji, M., et al.* BiSrCaCu O intrinsic Josephson junction stacks with improved cooling: Coherent emission above 1 THz // Appl. Phys. Lett. 2014. V. 105 Art. ID 122602.

6. *Kashiwagi, T., et al.* A high-Tc intrinsic Josephson junction emitter tunable from 0.5 to 2.4 terahertz // Appl. Phys. Lett. 2015. V. 107 P. 082601.

7. *An, D. Y., et al.* Terahertz emission and detection both based on high-Tc superconductors: Towards an integrated receiver // Appl. Phys. Lett. 2013. V. 102. Art. ID 092601.

8. *Sekimoto, S., et al.* Continuous 30 W terahertz source by a high-Tc superconductor mesa structure // Appl. Phys. Lett. 2013. V. 103. Art. ID 282601.

9. *Koshelets, V. P., and Shitov, S. V.* Integrated superconducting receivers // Supercond. Sci. Technol. 2000. V. 13. No. 5. P. R53–R69.

10. *Koshelets, V. P., et al.* Superconducting integrated THz receivers: Development and applications // Proc. SPIE. 2010. P. 78540J-1–78540J-13.

11. *Kinev, N. V., Filippenko, L. V., Li, M. Y., Yuan, J., Wang, H. B., and Koshelets, V. P.* Spectral properties of a terahertz oscillator based on the BiSrCCuO mesastructure // Radiophysics and Quantum Electronics, 2014, V. 56, No. 8–9, P. 582-590.

12. *Koshelets, V. P., et al.* Superconducting integrated terahertz spectrometers // IEEE Trans. Terahertz Sci. Technol. 2015. V. 5. P. 687.

13. *Sun, H., et al.* Terahertz Spectroscopy of Dilute Gases Using BiSrCaCuO Intrinsic Josephson Junction Stacks // Phys. Rev. Applied. 2017. V. 8, P. 054005.

SubTHz Arrays of Planar Antennas with SINIS bolometers for BTA

G. Yakopov[4], M. Tarasov[1], A. Gunbina[2,5], M.Mansfeld[2,5], R. Yusupov[1], V. Edelman[6], and V. Vdovin[2,3,5]

[1]V.Kotelnikov Institute of Radio Engineering an d Electronics RAS
[2]Institute of Applied Physics RAS
[3]P.N. Lebedev Physical Institute of the Russian Academy of Sciences
[4]Special Astrophysical Observatory RAS
[5]Nizhny Novgorod State Technical University n.a. R.E. Alekseev
[6]P.Kapitza Institute for Physical Problems RAS

We have investigated the optical and spectral response of a 350 GHz receiver made of annular antenna array with SINIS bolometer elements. Receiver is intended for using at Big Alt-Azimuthal Telescope (BTA). Samples were measured in a dilution cryostat at temperatures in the range 80-400 mK. Voltage responsivity approaches $3*10^9$ V/W. Spectral bandwidth in 230-380 GHz range for single array was measured using Backward Wave Oscillator source.

BTA SAO RAS

The BTA-6 is a 6-metre aperture optical telescope at the Special Astrophysical Observatory located in the Zelenchuksky District on the north side of the Caucasus Mountains at an altitude of 2070 m above sea level. Photo and schematic picture of BTA is presented in Fig.1. The mounting of a cryostat with receiving array is supposed in the Nasmyth focus. The equivalent focus length is 184 meters and diameter of diffraction image is 60 mm. For matching receiving array with incoming radiation we can use horn with large aperture (up to 60 mm) or lens with the same diameter or decreasing of focal length of 24 times by using a large lens.
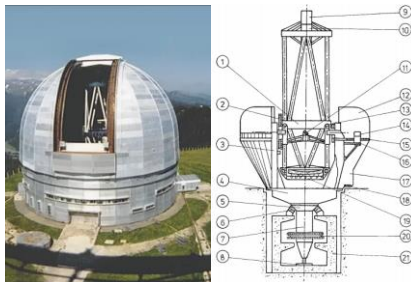

Fig.1. The photo of BTA (left) and schematic picture (right): 1- middle unit; 2 - worm gear; 3 - elevator; 4 - rotation support platform; 5 - spherical support of vertical axis; 6 - spherical pads; 7 - vertical axis; 8 - lower bearing; 9 - observer's cage; 10 - prime focus unit; 11 - flat mirror; 12 - platform cover; 13 - oil pads; 14 - main spectrograph; 15 - observing platform; 16 - support for spectrograph; 17 - pier; 18 - 2m camera mirror of main spectrograph; 19 - primary mirror cell; 20 - spur and worm gears; 21 - reinforced concrete.

Matching of incoming signal with receiver array

Receiving array can be matched with incoming signal using arrays of horns, quasi-optical lenses or distributed absorbers. The main advantages and disadvantages of using feedhorns and filled arrays are represented in [1] and in table.

Feedhorns	Filled array
Advantages	**Advantages**
a) Provides maximum efficiency for detection of a point source with known position; b) the bolometer angular response is restricted to the telescope, giving good stray-light rejection; c) the susceptibility to electromagnetic interference can be controlled — the horn plus integrating cavity act as a Faraday enclosure; d) the number of detectors needed to fill a given array field of view is minimized	a) Provide a higher efficiency for mapping observations; b) they allow full sampling of the instantaneous field of view of the array by use of pixels of 0.5Fλ or smaller, making jiggling unnecessary; c) they yield, for a 0.5Fλ array, a slightly narrower beam profile on the sky for a given telescope size owing to the stronger illumination of the outer parts of the telescope
Disadvantages	**Disadvantages**
a) In order to achieve full spatial sampling of the sky, even for a region smaller than the array field of view, jiggling or scanning are needed, which complicates the observing modes; b) the efficiency for mapping is considerably less than the ideal value	a) the background power per pixel is lower than for the larger feedhorn coupled detectors, typically by a factor of 4 –5, yielding a photon noise NEP that is lower by a factor of 2 or more, and thus more difficult to achieve; b) the detectors are much more vulnerable to stray light because of the very broad pixel angular response — by a factor of $\pi F^2/4$, assuming a pixel beam solid angle of π steradians; c) the vulnerability to electromagnetic interference is also greater owing to the naked array architecture; d) the need for more detectors to fill a given field size

In case of using immersion lens close to elliptical lens [2] allows to remove substrate modes and to increase gain coefficient of planar antenna. The spherical wave transforms in plane wave by mounting the source in the second focus.

We suggest two types of arrays for using at BTA: half-wave antenna arrays (with back-to-back horn) and metamaterial arrays (with lens). A single element is an annular antenna with two (or more) SINIS-bolometers (Fig.2). Schematic image of matching such arrays with incoming radiation are presented in Fig.3.

A metamaterial is made of a periodic array of subwavelength metallic resonators that are collective-

ly coupled to the free space excitation. In the case of small antennas the matrix can be made more wideband and much smaller that allows placing it in the waist of a single-mode horn or in the focus of immersion lens.
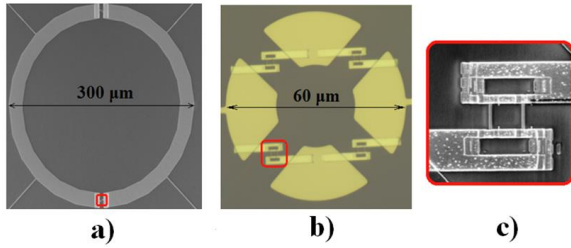

Fig.2. The single elements of investigated structures for 345 GHz receiver arrays: a) Half-wave antenna, b) Metamaterial, c) SINIS-bolometer
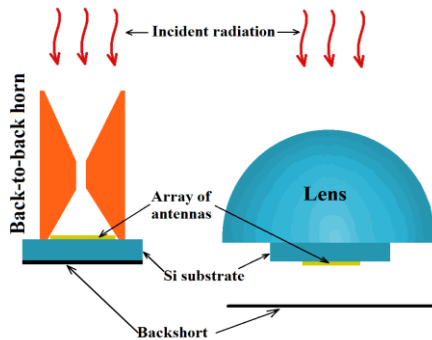

Fig.3. Schematic image of measurements such arrays: half-wave antenna array with back-to-back horn (left) and metamaterial array with lens (right)

Experimental setup and results

Quasistatic optical response to incoming radiation was measured in dilution cryostat [3] using cold black body (BB) source made of NiCr film on sapphire substrate. Source was equipped with thermometer, connected to current source and mounted on 2.7 K stage. For spectral response measurements we use a 230-380 GHz Backward Wave Oscillator (BWO) illuminating the antennas array via optical window and 3 neutral density filters with transmission below -10 dB placed at radiation shields 100 K, 3 K, 0.3 K temperature stages. Two channels were measured simultaneously by lock-in amplifier, one for signal from bolometer, and another from pyroelectric detector that is monitoring level of the incoming power. Schematic pictures of experimental setup are presented in Fig.4. Results of spectral and optical response measurements are presented in Fig.5,6.
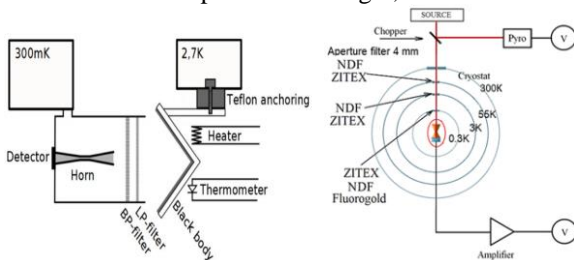

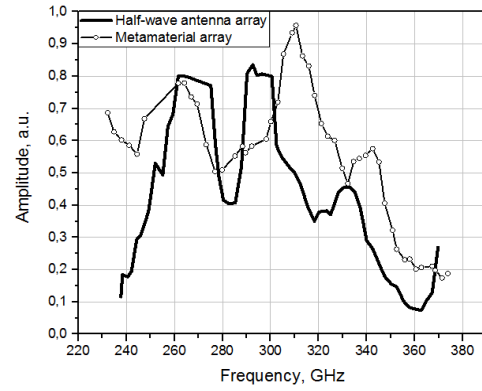**Fig.4.** Experimental setup with cold BB (left) and with BWO source (right)

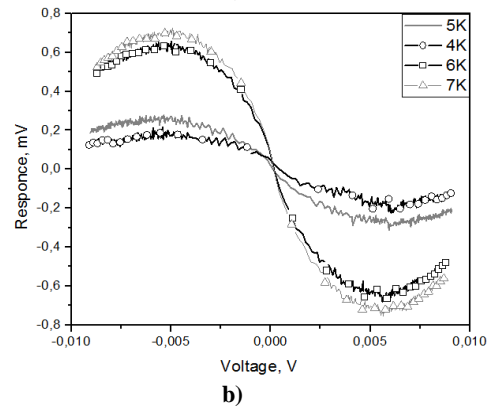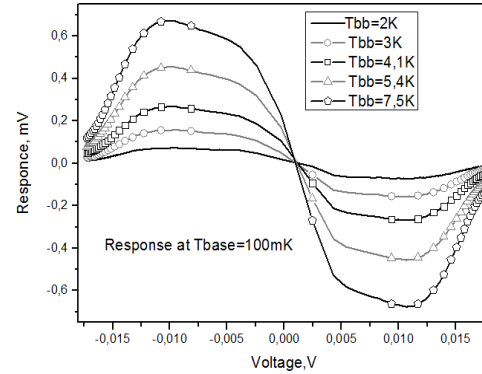**Fig.5.** Spectral response of investigated structures

Fig.6. Voltage response of metamaterial array (a) and half-wave antenna array (b) to blackbody radiation

References

1. *M.Griffin, J.Bock, W.Gear*, Relative performance of filled and feedhorn-coupled focal-plane architecture, Applied Optics, v/ 41, No31, 6543-6554 (2002)
2. *D.F.Filipovic*, Double-slot antennas on extended hemispherical and elliptical silicon dielectric lenses, IEEE Trans. Microwave Theor. and Techn., vol. 41, No10, pp.1738-1749 (1993).
3. *V. S. Edelman*, A dilution microcryostat-insert, Instrum. Exp. Tech. **52**, N2, 301-307 (2009), DOI: 10.1134/S002044120902033X.